Description of Main S&T Results/Foregrounds (632433 OFS-MOTOR)

The research has reached a successful completion, following carefully the work plan laid out in the proposal with key deliverables/milestones having been successfully achieved as detailed below.

WP1: Design of the sensor system and test bed to meet CFP objectives

<u>Deliverable 1.1 (completed).</u> Review report on the state-of-the-art in fibre optic distributed sensing solutions and preliminary design review of the sensor system and of the test bed.

At the beginning of the project, a comprehensive *review report* on the state-of-the-art in fibre optic distributed sensing solutions was generated and shown in Table 1.1.

Table 1.1 Review report on the state-of-the-art in fibre optic distributed sensing solutions
Different optical methods [1.1] based on Bragg scattering, cantilevered beam, and light modulating measurement (LMM) have been reported for potential motor condition monitoring, but unfortunately the technique has not yet been widely used because of incorrect results obtained either due to improper location of the sensors installed or tests undertaken only at ambient temperature.   City University London has undertaken some **pilot studies**, exploring the potential of using FBG techniques by undertaking a set of 'proof of concept' experiments.   *Temperature profiling using FBGs*   *(a) Temperature sensing principle*   A FBG formed within a fibre behaves like a 'notch filter', which reflects the light at a wavelength termed the Bragg wavelength (λ_B) that satisfies the Bragg condition, given in equation (1.1). $\lambda_B = 2n_{eff}\Lambda$ (1.1)   where n_{eff} is the effective refractive index of the fibre core and Λ is the grating period, where *both* are affected by strain and temperature variations, a feature that is reflected in the sensor design.   Due to temperature changes, the grating-period varies as a result of the thermal expansion coefficient of the material and the thermo-optic effect creates a change in the effective refractive index of the fibre-core. Thus, the shift of the Bragg wavelength, $\Delta\lambda_B$, can be expressed as $\Delta\lambda_B / \lambda_B = (1-\rho_e)(\Delta L/L) + \Delta n/n$ (1.2)   where ρ_e is the photo-elastic coefficient of the fibre, $(\Delta L/L)$ is the strain induced in the fibre arising from the thermal expansion and $\Delta n/n$ is the fractional refractive index change due to the thermo-optic effect. If the thermal-strain and the fractional effective refractive index changes are assumed to be proportional to the applied temperature, equation (1.2) may be rewritten as $\Delta\lambda_B / \lambda_B = [(1-\rho_e)\alpha + \zeta]\Delta T$ (1.3)   where $\alpha = (1/L)(dL/dT)$ is the thermal expansion coefficient and $\zeta = (1/n)(dn/dT)$ is the thermo-optic co-efficient of the material. Combining equations (1.2) and (1.3), the thermo-optic coefficient of the fibre can also be determined, which can be expressed as a function of the Bragg wavelength as $\zeta = (1/n)(dn/dT) = (1/\lambda_B)(d\lambda_B/dT) - (1-\rho_e)\alpha$ (1.4)   *(b) Quasi-distributed temperature sensing system*   In order to map a temperature profile in a motor, a quasi-distributed FBG-based temperature sensor system, as illustrated in Figure 1.1.1, is used to monitor temperature variations at multiple sensing points (FBGs), each being encoded with a distinctive Bragg wavelength for location identification. As a result, each grating period and the fibre core effective refractive index, given in equation (1.1), will be modulated by the temperature distribution on the motor, thus resulting in the corresponding Bragg wavelength shifts as given in equation (1.3).

Compared to the use of conventional thermocouple techniques, optical fibre distributed temperature sensors have shown considerable advantages in terms of being immune to electromagnetic interference, ease of handling and the capability of multiplexing a series of such fibre Bragg gratings (i.e. temperature sensors) within a single length of fibre, co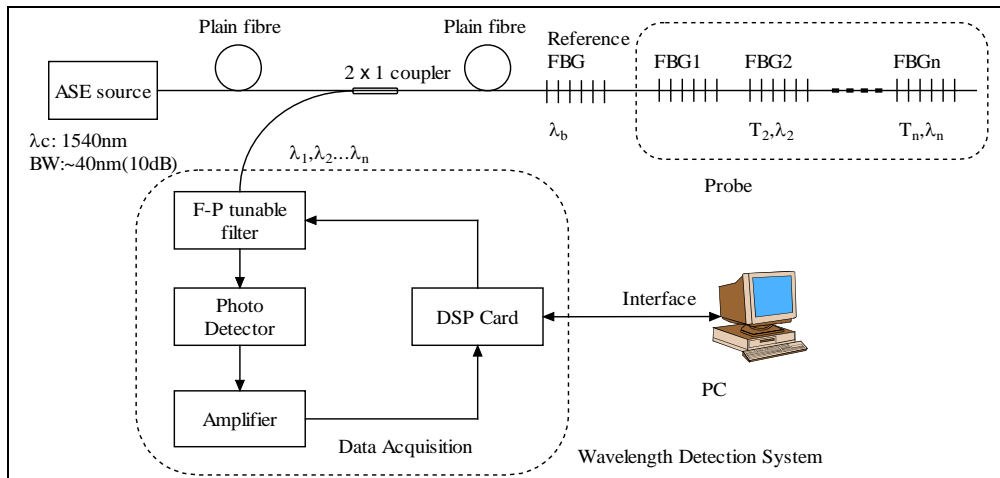upled to a single source (either a swept laser source or a broadband light source coupled with a F-P tunable filter) and interrogated by a single detector. A wavelength division multiplexing (WDM) technique [1.2] is used to address the gratings and yield both the temperature values of multiple sensors and, through prior calibration, their physical locations on the surface of the motor.

Figure 1.1.1 A quasi-distributed FBG-based temperature sensor system

(c) Preliminary tests on the motor

Figure 1.1.2(a) shows an electric motor stator instrumented with 17 FBGs mapped on the inner circumference and Figure 1.1.2 (b) the zoom-in photo, showing both the FBG sensors and their fibre connection to an interrogation system, as illustrated in Figure 1.1.1. For cross-comparison, several thermocouples are also included in the preliminary test for temperature measurement.
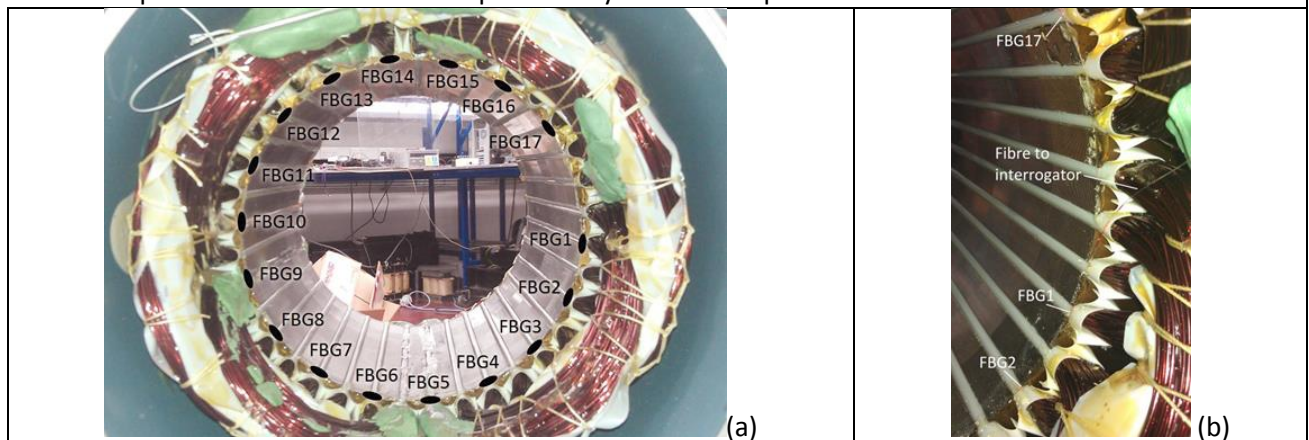

Figure 1.1.2 (a) An electric motor instrumented with 17 FBGs mapped on the inner circumference of a stator; (b) zoom-in picture, showing both the FBG sensors and their fibre connection to an interrogator
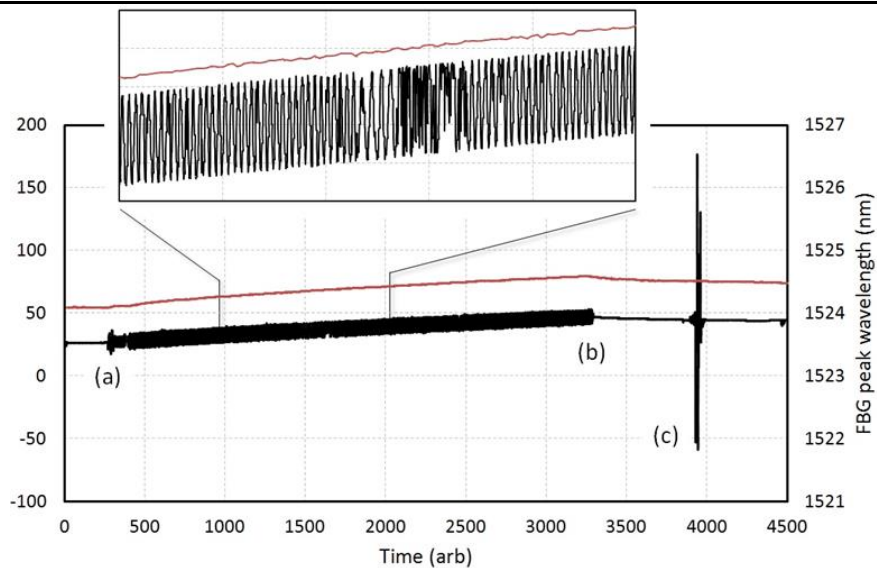
Figure 1.1.3 Preliminary experimental data obtained from a FBG-based temperature sensor (red), in cross-comparison with that from a thermocouple (black)

Figure 1.1.3 shows the preliminary experimental data obtained from a FBG-based temperature sensor, in cross-comparison with that from a thermocouple, when the motor is under various operational conditions. At (a), the power injected into the motor is ramped up and it is noticeable that the FBG (red curve) and thermocouple (black curve) both indicates the increase of temperature showing that the motor is heated up when it is in operation. However, the signal from the thermocouple (not shielded) is far noisier than that from the FBG, confirming that the optical sensor is immune to the EM interference, unlike the conventional thermocouple. At (b), the motor is switched off and both sensors indicate the motor cooling process, together with the disappearance of the EM effect on the thermocouple. At (c), the motor is switched on again, but unlike (a) in which the power is injected slowly, the step change of the power in this case leads to a massive scale of noises appeared at the thermocouple signal, but not at the optical sensor signal, demonstrating a clear advantage of optical fibre sensors being used for measurement in an environment where electromagnetic interference becomes an importance issue to conventional electrical sensors.
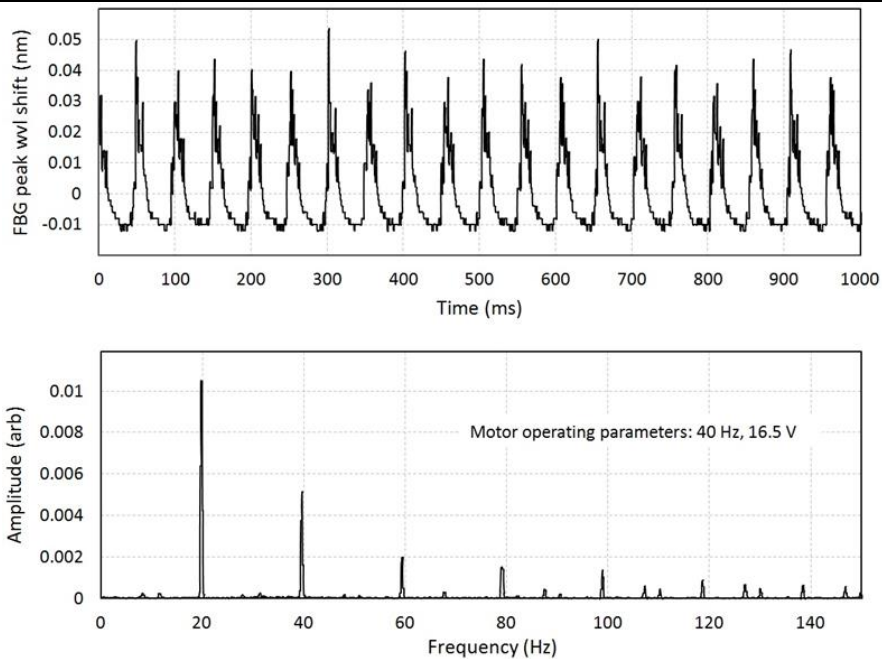
Vibration monitoring using FBGs

Figure 1.1.4 Vibration monitoring data from one FBG installed on the motor operating at a frequency of 40 Hz

Figure 1.1.4 plots the Bragg wavelength shift of one FBG installed on the motor in response to vibration,

which leads to the grating period Λ variation, as indicated in equation (1.1). The motor is operated at a frequency of 40Hz (with a power level of 16.5V), without any load and the FFT spectrum in Figure 1.1.4 indicates the fundamental frequency to be 20Hz and this matches well with the expected performance of a 4-pole machine. Figure 1.1.5 shows the vibration monitoring data obtained from one FBG installed on the motor when operating at a frequency of 40 Hz at different current levels, but with the rotor being locked. It is understandable that no pulsed transient signal is being picked up, but the FFT data indicates a dominant frequency of 80Hz, irrespective of the driving current/power, which again matches well with the expected performance of a 4-pole machine when its load reaches maximum.
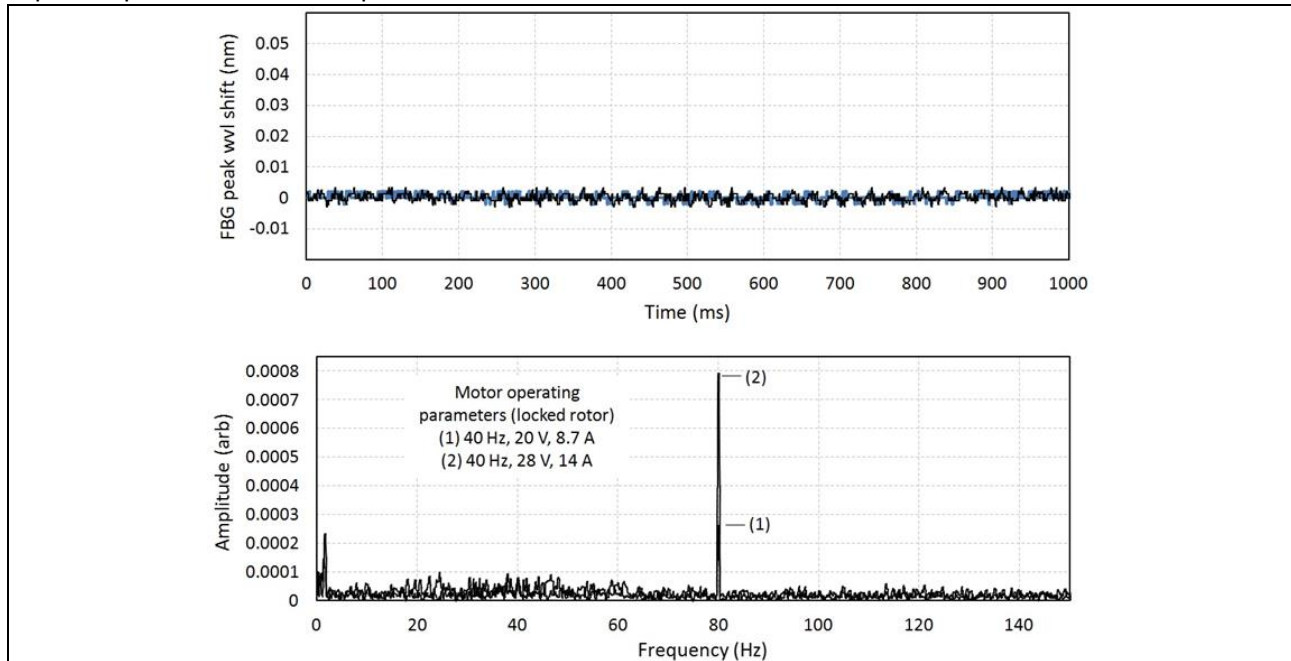

Figure 1.1.5 Vibration monitoring data from one FBG installed on the motor operating at a frequency of 40 Hz at different power levels, but with the rotor being locked

References:
[1.1]   M Sasic, H Jiang, G C Stone, "Requirements for fiber optic sensors for stator endwinding vibration monitoring", *2012 IEEE International Conference on Condition Monitoring and Diagnosis*,
23-27 September 2012, Bali, Indonesia
[1.2] A. Othonos and K. Kalli, *Fiber Bragg gratings: fundamentals and applications in telecommunications and sensing*, Artech House Boston, 1999

This is followed by the detailed discussions made with the Topic Manager which leads to the generation of a formal *design report* shown in Table 1.2, detailing the preliminary design of the novel sensor system and of the test bed, based on the *comprehensive review* written and agreed by both parties.

During the whole project period, multiple discussions with the Topic Manager and a test bench manufacturer (IMC Berlin) have been made with an attempt both to meet the test bed specifications set in Table 1.2 and to be within the project budget. But due to the significant delay induced by negotiation, a tele-conference was arranged between the Project Coordinator, the Topic Manager and the Project Manager. It was agreed at the tele-conference that the Topic Manger was to set up the test bench by ordering bits and pieces in order to meet the specifications given in Table 1.2, thus to ensure the timely delivery of this two-year project.

Table 1.2 Design of the sensor system and of the test bed	
Maximum rated speed:	10,000rpm
Torque at Max rated speed:	30Nm
Torque at zero speed:	300Nm
Torque beyond 10krpm:	Power limited at 30kW

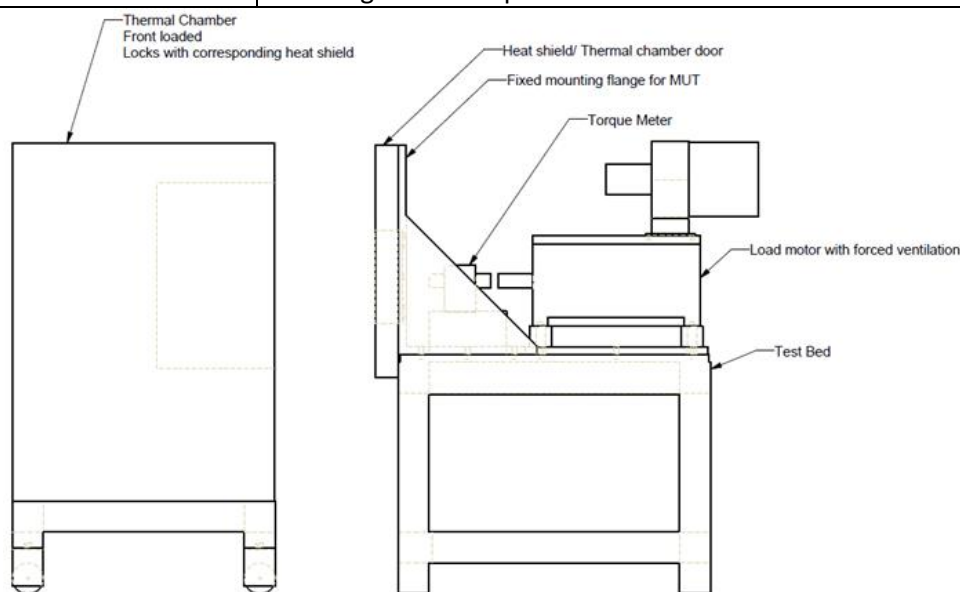| Torque measurement:	a. Via directly coupled, test bed mounted torque transducer b. 4-20mA and digital output
Load drive type:	4 quadrant
Coupling to MUT:	a. direct via torque transducer (no gear box) b. two sets of flexible coupling to be provided at both ends of the Torque transducer c. 40mm diameter (shaft)

Others	a. Test bed dimensions:1000mmx1800mm
	b. Adjustment for various MUT shaft length to be made available for adjustable location of the load machine
	c. Thermal chamber for MUT and converter
	  i. Temperature range: from -45°C to 250°C (alternatively: -30°C to 200°C)
	  ii. Mounting option will have to be decided
	d. A proposed test bed design is shown in Figure 1.2.1

Control cabinet options:	a. Local and remote start/stop b. Local and remote state (run, stop, trip) indication c. Local and remote set point (V, I, T) d. Local display for real-time set point values e. Local display for real-time shaft speed f. Local/remote key g. Local emergency stop x2 (cabinet and test bed) h. Load power monitoring: V, I, P, VA, VAr, cos(phi) i. USB (alternatively GBIP/Can) bus interface for both drive and power monitor parameters j. Oscilloscope outputs (via amplifiers) for terminal voltage and current of load machine (+/- 5V or +/- 10V)
Control for load motor	a. V/f (standard control method) b. Vector control with encoder (rotor flux orientated, encoder needed to verify system speed) c. Torque control
Control for MUT	Via UON standard DSK platform (DSP + FPGA module, under development)
General remarks	a. Load motor and torque transducer should be sitting on a slider b. No gear box required

Figure 1.2.1 Test bed layout draft with the motor under test sitting in a temperature controlled chamber and the load machine having an axial degree of freedom to cater for various MUT shaft lengths

WP2: Development of all-in-one optical fibre sensor system

Deliverable 2.1 (Completed). An all-in-one optical fibre multi-parameter sensor system has been successfully developed for monitoring electrical motor drives. This includes

- Successful 3-D temperature profiling of the rotor using the temperature data obtained from the FBGs mapped onto the surface of the rotor. This 3-D imaging is extremely useful for the hot-spot identification in particular for PMAC motors as they are temperature sensitive.

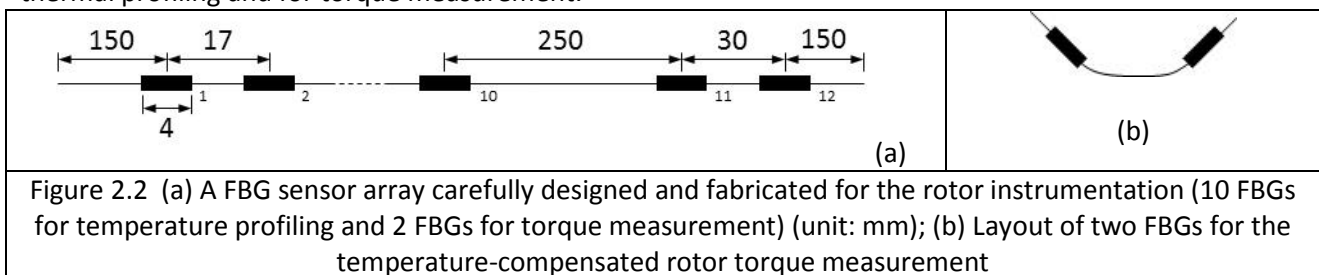Figure 2.1. Exemplary plot showing the rotor temperature distribution
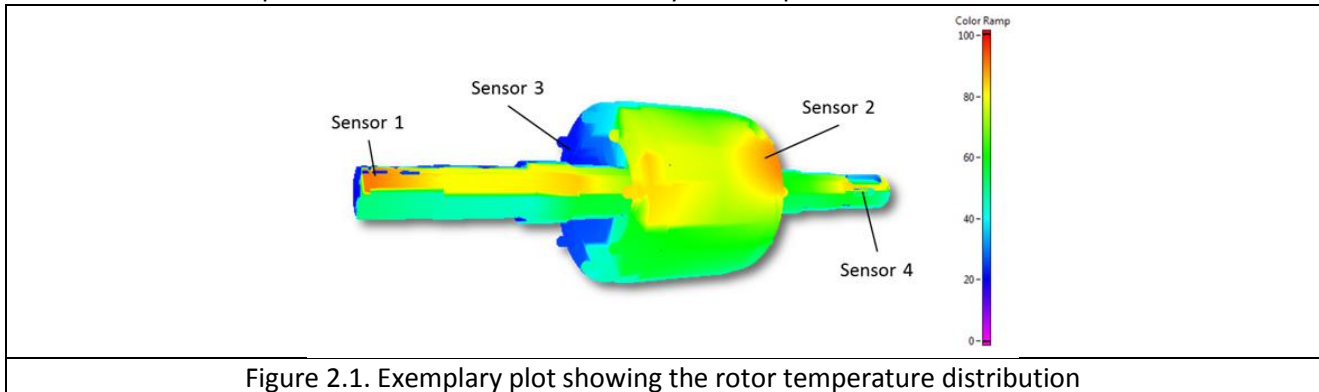
Figure 2.1 shows some simulation data illustrating how a 3-D thermal profile of a rotor can be obtained based on four sensing points (FBGs) installed on the rotor, after their calibration against standards under controlled temperature conditions. This is followed by a careful design and fabrication of arrays of FBGs, as shown in Figure. 2.2. This is for instrumenting the rotor of a PMAC Machine (NFSM SI 2000), both for thermal profiling and for torque measurement.

Figure 2.2 (a) A FBG sensor array carefully designed and fabricated for the rotor instrumentation (10 FBGs for temperature profiling and 2 FBGs for torque measurement) (unit: mm); (b) Layout of two FBGs for the temperature-compensated rotor torque measurement

As shown in Figure 2.2 (a), a fibre with a total length of 800 mm, carrying 10 FBGs for thermal profiling and 2 FBGs for torque measurement, is prepared for the instrumentation of a rotor of a PMAC motor. Each FBG is encoded with a distinctive wavelength with a sensor length of 4 mm. The sensor interval between 10 FBGs used for temperature measurement is 17 mm. The distance between the last temperature FBG sensor and the first torque FBG sensor is 250 mm, taking into account the dimension of the PM rotor. The interval between the two torque FBGs is set to be 30 mm, allowing for their proper installation, i.e. ±45° with reference to the central axis of the PM rotor, as shown in Figure 2.2 (b), allowing for temperature-compensated torque measurement. The sensor layout of the instrumented PMAC rotor is shown schematically in Figure 2.3 (a) while Figure 2.3 (b) shows a photo of the concerned sections of the instrumented rotor. This task has proven particularly challenging because, in contrast to the induction machine used to evaluate the feasibility of this sensing technique, the rotor is quite violently pulled toward the stator when the former is inserted into the latter. This has been appropriately addressed by cutting a groove into the insulation material of the magnets into which the fibre was then "buried" and covered with resin. Using this approach, the fibre has survived the whole rotor insertion process without any problem.
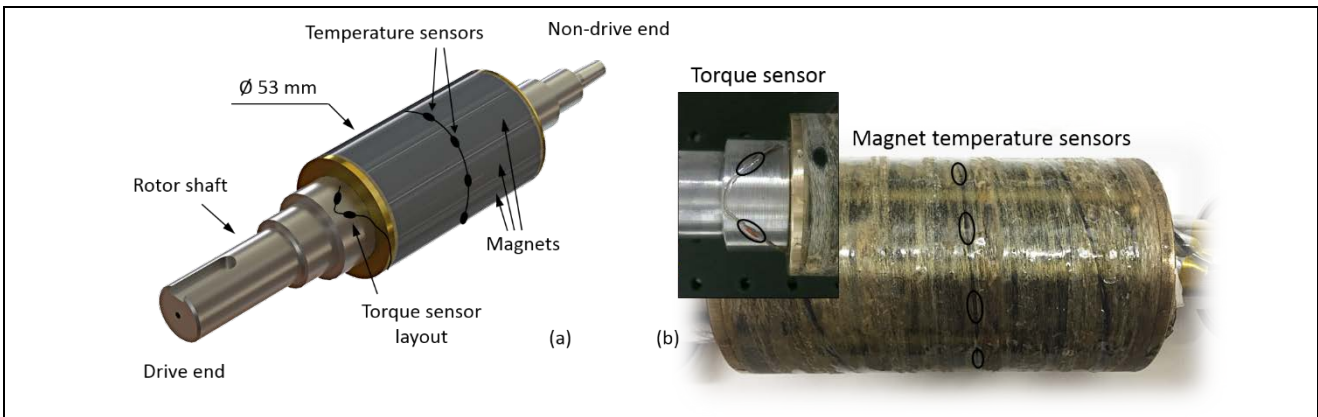
Figure 2.3 (a) Schematic diagram of an instrumented PM rotor; (b) photo of the instrumented PM rotor

Figure 2.4 shows the sensors designed and fabricated for the PM motor stator. Figure 2.4 (a) shows the design of a sensor array installed circumferentially inside the stator. The fibre is of a length of 750 mm, carrying 12 FBGs of 3 mm each, with an interval of 14.5 mm. In addition, two fibres are installed into the end-windings of the stator for thermal profiling. Figure 2.4 (b) shows the design of the latter fibres each of 1200 mm length, carrying 12 FBGs of 4 mm each at a spacing of 28 mm. This configuration would allow 2 FBGs to be installed in each stator slot. Therefore, altogether there are 36 FBG sensor points to be mapped into the stator circumferentially and along the end-windings for simultaneous measurement of multiple parameters.

Figure 2.4 (a) FBG sensors to be circumferentially mapped onto the PM motor stator; (b) sensors to be installed along end-windings of the PM motor stator; (unit: mm)

The FBG locations for thermal profiling are marked by white arrows in Figure 2.5 (b), i.e., two sensors per stator slot at 1/3 and 2/3 of the stator core length. At the end of the stator core the fibres are looped around, skipping one slot at a time (Figure 2.5 (a)). The crosses and circles in Figure 2.5 (a) indicate the fibre's routing direction, i.e., beginning from the start point (S), the two fibres were routed towards the drive end (DE) of the machine, then looped around at the drive end (broken line), routed back to the non-drive end (NDE), looped around at the non-drive end (solid line) and so on. The bare fibres are covered in resin along the length of the stator core while the loops at either end were spot glued to the windings in order to keep the fibres away from the spinning rotor.
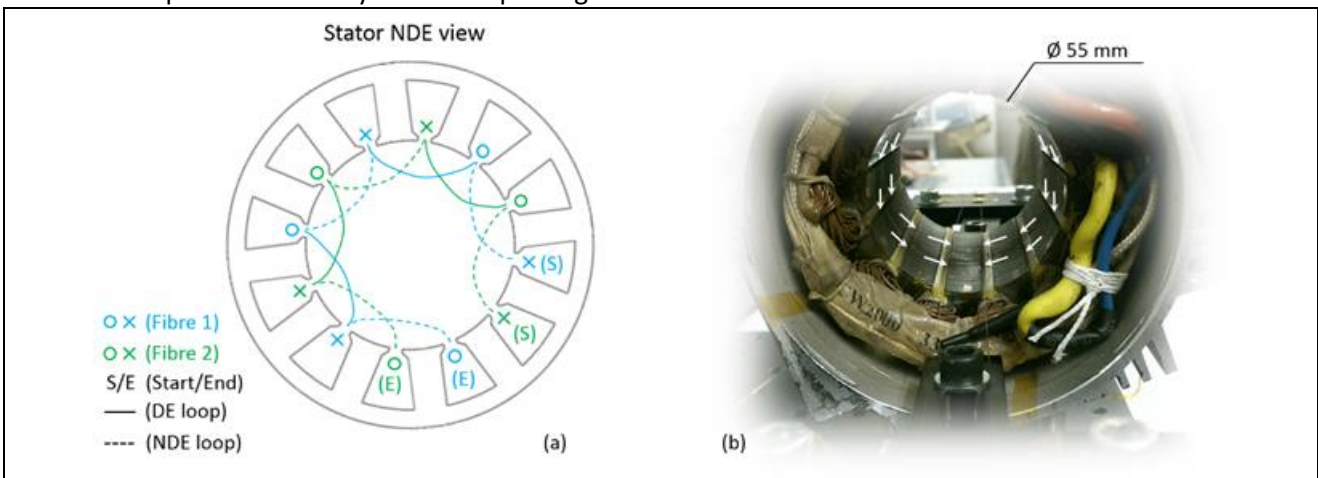

Figure 2.5. (a) Schematic diagram of the sensor layout along the end-windings of the stator for thermal profiling; (b) the stator instrumented with temperature sensor arrays.

After the completion of the instrumentation and PMAC motor assembly discussed above, the FBGs used for temperature monitoring were calibrated by putting the motor in a climate chamber, as shown in Figure 2.6, and running a pre-programmed temperature cycle (20°C to 70°C in steps of 10°C).
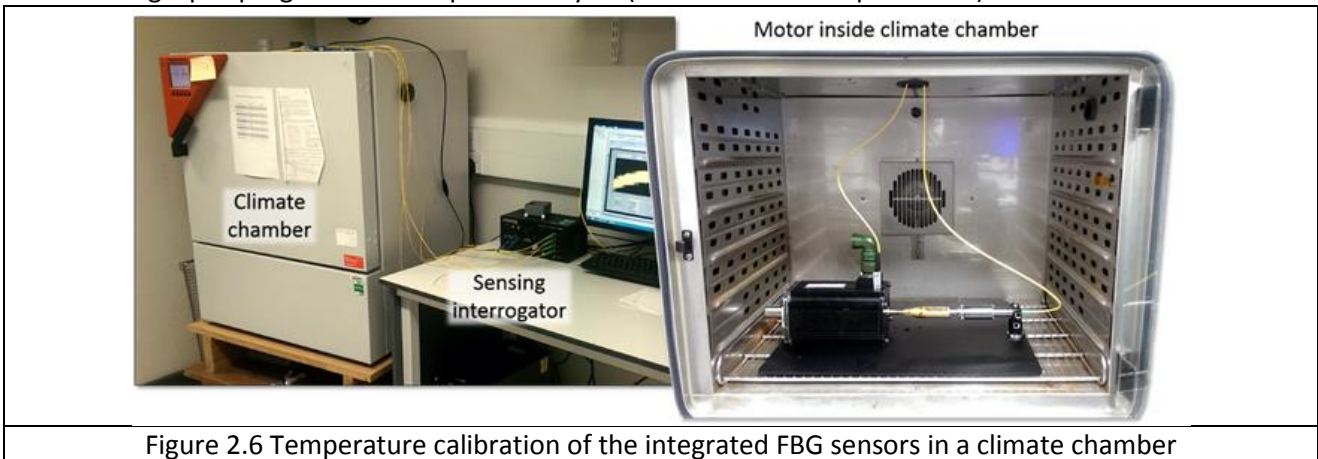

Figure 2.6 Temperature calibration of the integrated FBG sensors in a climate chamber

The collected data from each FBG at each temperature step were averaged and then individually fitted using a linear least squares algorithm as shown in Figure 2.7.
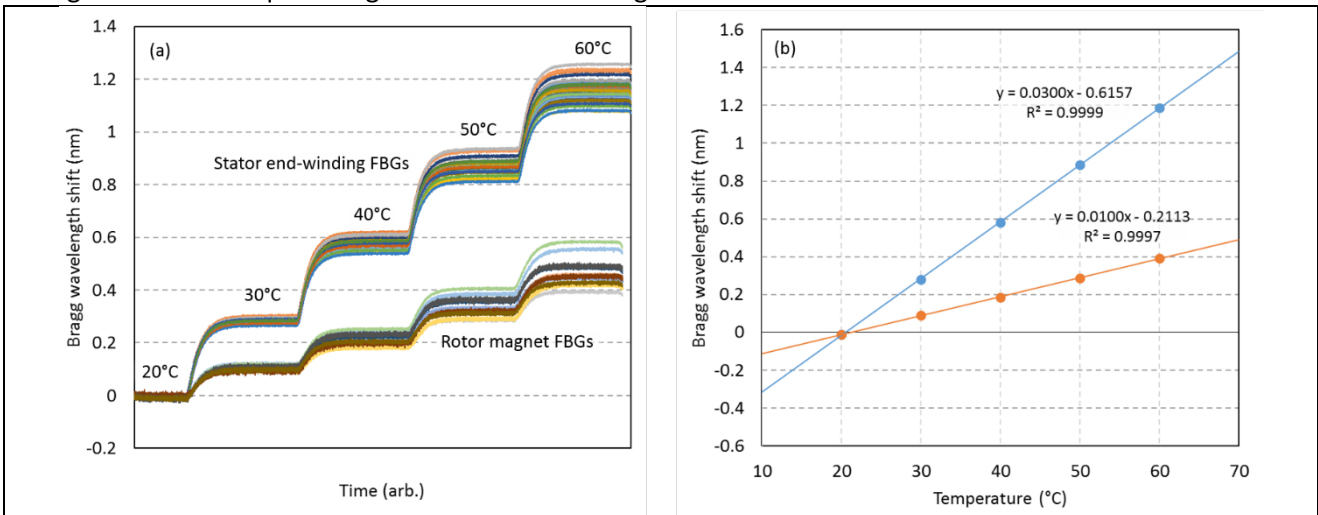
Figure 2.7 Temperature calibration curves. (a) Bragg wavelength shift of all 34 FBGs used for temperature profiling; (b) Linear fitting of the temperature-dependent Bragg wavelength shifts of two exemplary FBGs

Figure 2.7 (a) shows the temperature-dependent Bragg wavelength shifts of the 34 FBGs (24 in the stator and 10 the rotor), used for rotor and stator temperature profiling, at the temperature intervals mentioned above. It can be observed from Figure 2.7 (a) that the FBGs attached to the stator end-windings exhibit approximately three times the wavelength shift as the ones attached to the rotor magnets. This is due to the different thermal expansion coefficients of the end-winding material and the magnet. Figure 2.7 (b) shows the fitted curves of two exemplary FBGs, with one installed on the end-winding of the stator and other on the rotor, to highlight their different temperature sensitivities (30pm/°C for the stator FBG versus 10pm/°C for the rotor FBG). It is also clear from the fitted curves that the temperature induced Bragg wavelength shifts are highly linear. With this information known, the absolute temperature T can be derived from the monitored Bragg wavelength λ_B of an FBG using equation (2.1), where c_T is the temperature coefficient or sensitivity of the FBG in *nm/°C,* obtained through calibration, and λ_{T0} is the Bragg wavelength at T0°C.

$$T = \frac{1}{c_T}(\lambda_B - \lambda_{T0}) \tag{2.1}$$

- Successful strain profiling and torque measurement.

This has been first achieved by mapping carefully the FBGs onto the surface of a rotor of a low-power test induction motor, with temperature compensation being taken into account. Figure 2.8 illustrates the

layout of 2 FBGs being attached to the rotor shaft at an angle of ±45°. This is designed specifically to compensate the temperature effect when torque is measured.
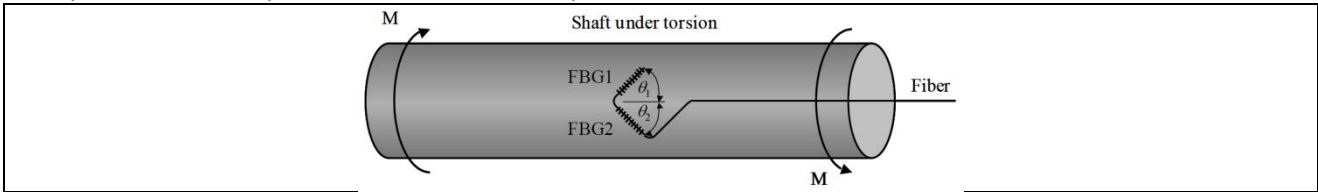

Figure 2.8. The layout of two FBGs used for temperature compensated torque measurement

It is the *differential* rather than *absolute* wavelength shifts between gratings that have been carefully monitored, thereby extracting the temperature-corrected torque/strain information. Figure 2.9(a) shows the spectral signal received from both FBGs, with each peak representing the Bragg wavelength of each grating. The distance between the two FBG peaks is a measure for torque whilst their absolute mid-point position is a measure for temperature. Figure 2.9 (b) shows clearly the linear relationship between the differential mode wavelength and the torque to be measured and the small residual temperature dependence has been fully compensated based on the mid-point temperature monitoring.
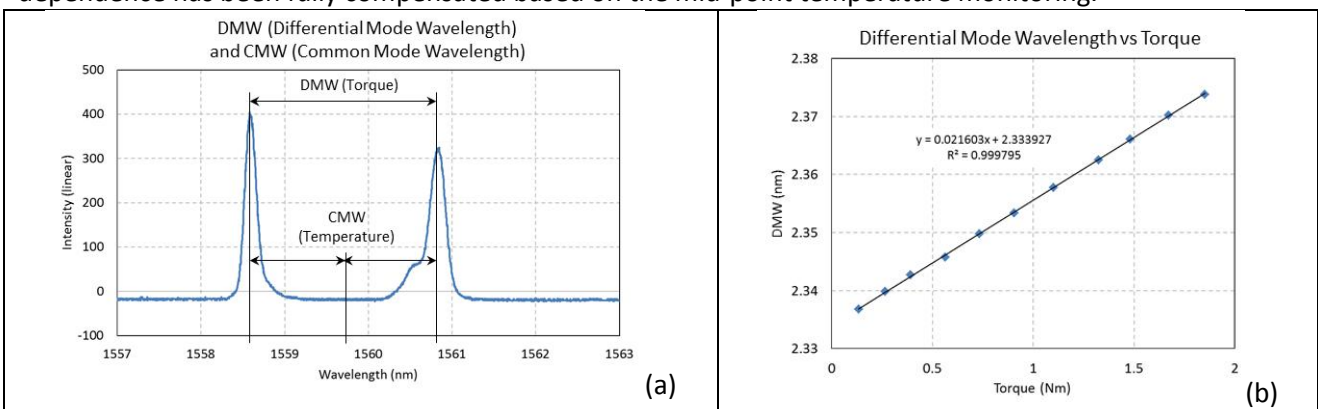

Figure 2.9. (a) Spectral signal received from the two FBGs used for the torque measurement; (b) The differential mode wavelength as a function of torque up to the maximum torque of the low-power test induction motor

In order to verify its effectiveness, a cross-comparison has been made with a commercial torque meter (Magtrol THMS 311/111), which is externally connected to the same rotor shaft, with different torque levels being generated using a magnetic brake. Figure 2.10 shows the results obtained and it is noticeable that a very good agreement has been reached.
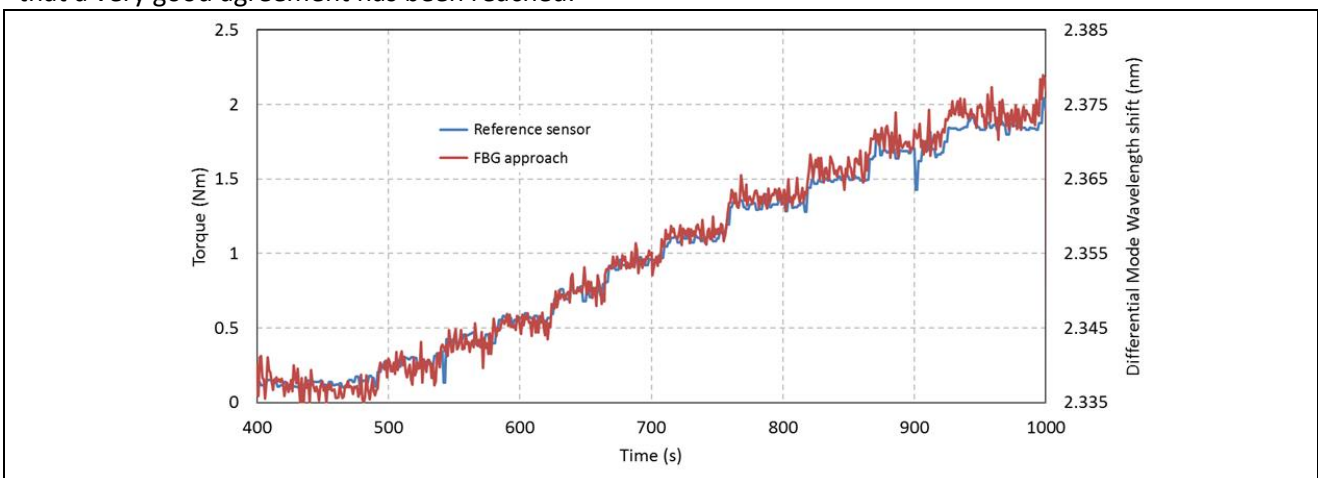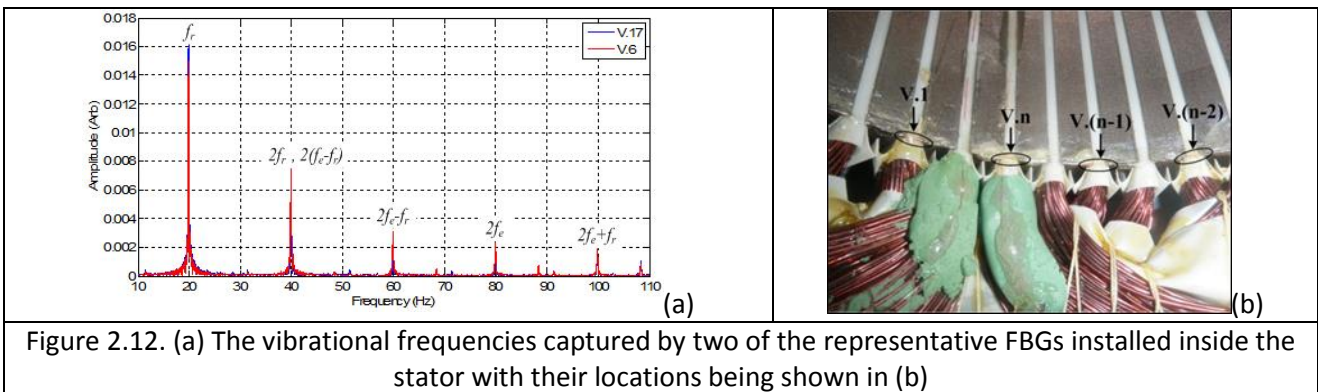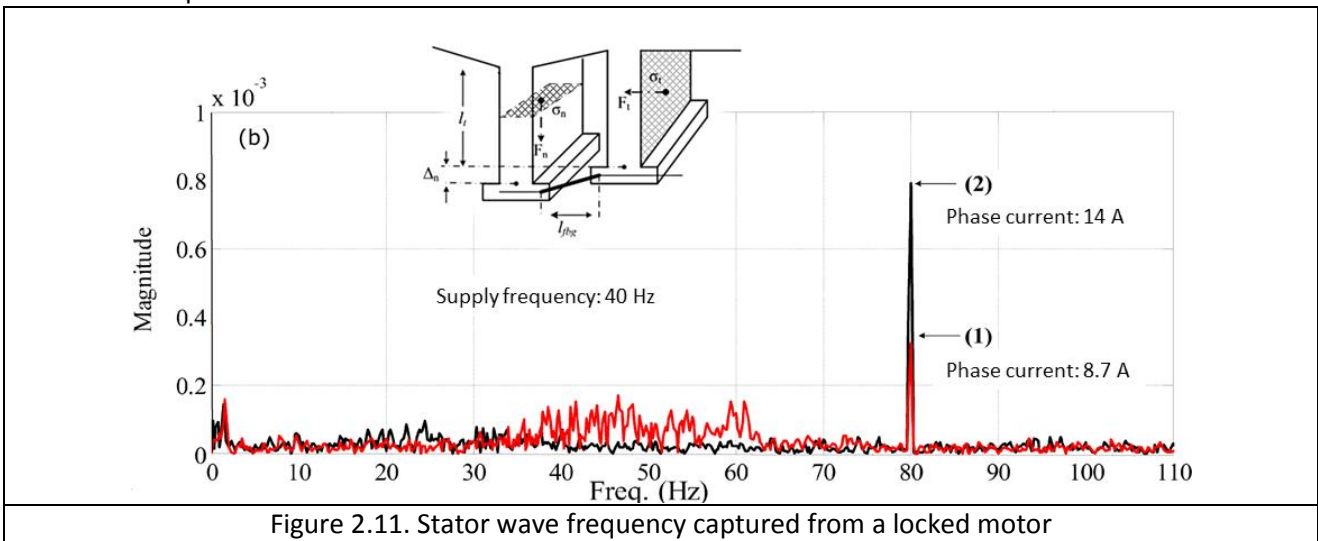

Figure 2.10. FBG torque sensor vs conventional torque reference sensor (Magtrol THMS 311/111)

Following the above successful evaluation of the temperature-compensated FBG-based torque sensor integrated into the induction motor, a similar sensor layout has been configured onto the rotor of a PMAC motor as shown in Figure 2.3 (b).

- Successful capture of the vibration signals of the motor when it is under varying loading conditions, ranging from the maximum loading, i.e. when the rotor is locked, to zero loading.

Figure 2.11 shows the signal obtained from a locked induction motor (max load) with the power supply switched on. The frequency peaks captured show the stator wave frequency at twice the supply frequency and no "mechanical" frequency at half the supply frequency has been observed at different phase current conditions. Figure 2.12 (a) shows the vibrational signals captured by the FBGs when the motor is running without any load and Figure 2.12 (b) shows the location of the FBGs installed on the inner surface of the stator to capture the vibrational frequencies. The fundamental frequency corresponds to the rotor speed (mechanical frequency) which is converted into an RPM signal. Knowing both the rotor speed and the stator wave frequency one can calculate another parameter, i.e., the slip, which is a crucial parameter for the closed loop control of the motor drive.

Figure 2.11. Stator wave frequency captured from a locked motor

Figure 2.12. (a) The vibrational frequencies captured by two of the representative FBGs installed inside the stator with their locations being shown in (b)

Following the above successful capture of the vibrational signal from the induction motor, Figure 2.13 (a) shows the configuration of a sensor array carrying 12 FBGs as illustrated in Figure 2.4 (a) being circumferentially attached to the stator core at the machine's non-drive end with the FBGs being located in between the 12 stator teeth. Figure 2.13 (b) shows an actual photograph of the instrumented section of the machine where the FBG locations are highlighted by white arrows. This sensor arrangement allows for the monitoring of the PMAC motor tooth elongation effect thus to capture the stator core vibrational wave.
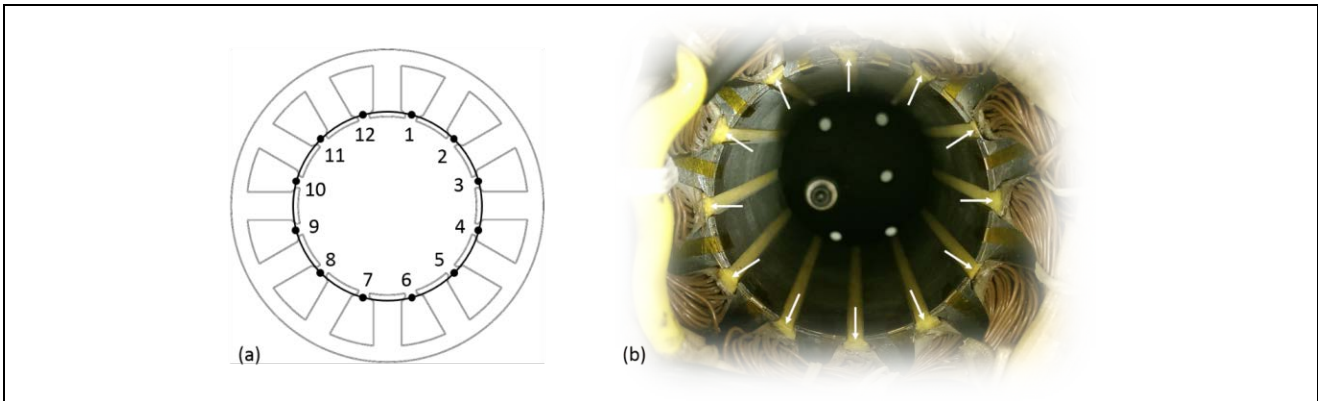
Figure 2.13 (a) Illustration of 12 FBGs being distributed circumferentially in between stator tooth pairs of a PMAC motor; (b) photo of the instrumented PMAC stator, allowing for monitoring of vibrational conditions.

- Successful measurement of the rotational speed/position based on the dynamic responses of the gratings and their phase relationships due to their different locations.

Accurate rpm measurement can thus be achieved based on the frequency components extracted from the vibration signal as shown in Figure 2.12. In order to verify its effectiveness, a cross-comparison has also been made with a commercial speed sensor (Magtrol THMS 311/111) when the motor is driven at different speeds. The results obtained are shown in Figure 2.14 where a very good agreement has been achieved.
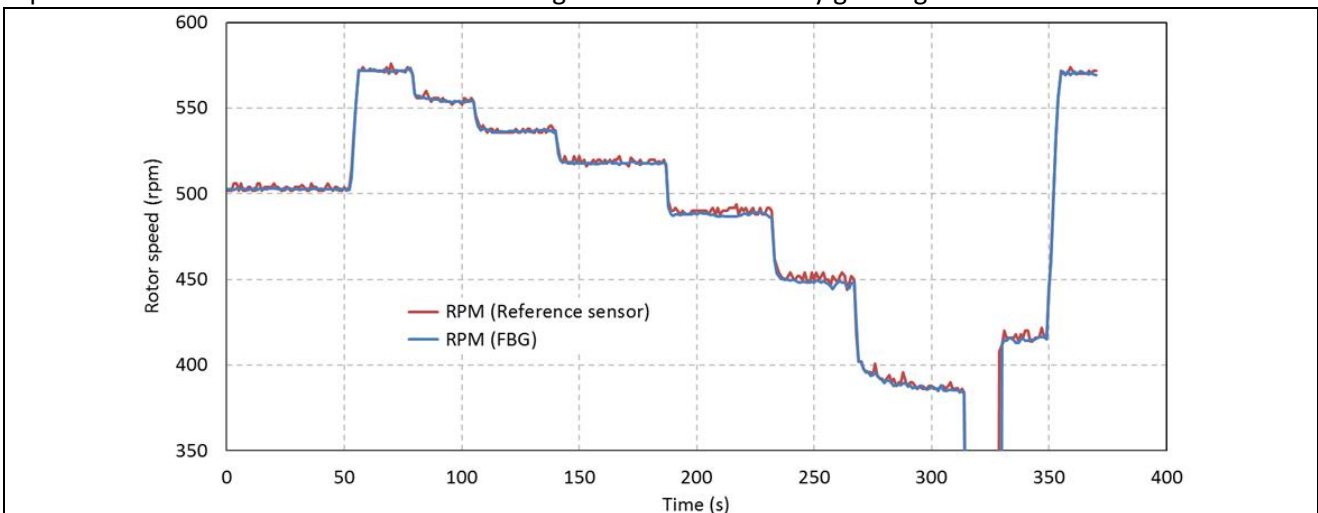

Figure 2.14. Cross-comparison between the FBG-based speed sensor and the commercial one

As indicated in Figure 2.15, there is a noticeable phase difference between the gratings installed circumferentially at different positions and this information can be used to extract the information of rotational position with reference to the specific locations of the sensors installed.
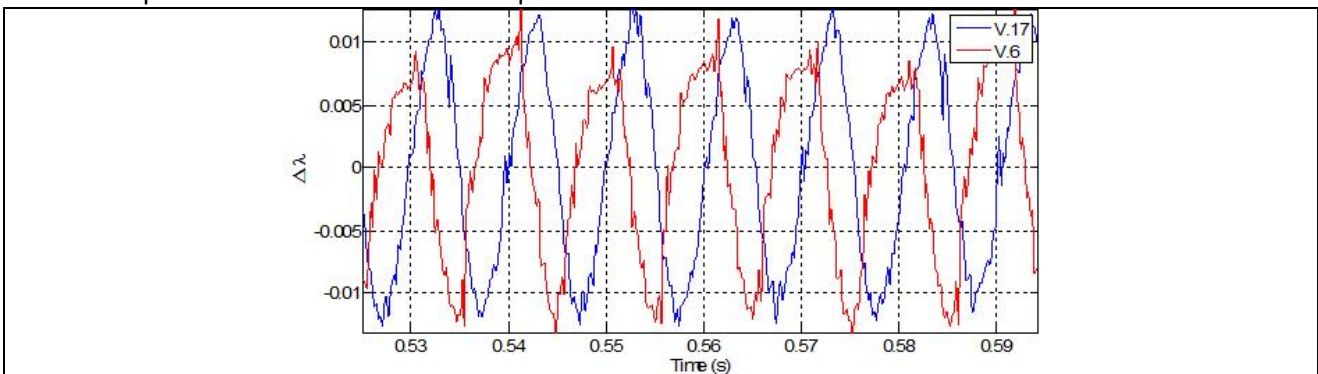

Figure 2.15 Determination of rotation position based on the phase shift of FBG signals with a reference to their specific locations

The data obtained from the sensors integrated into the PMAC stator, as illustrated in Figure 2.13, has further confirmed the effectiveness of using phase shift to track the rotational position. As shown in Figure 2.16, the dynamic Bragg wavelength shifts of the first four circumferentially mounted FBGs reveal consistent phase differences of approximately 3.5ms between adjacent sensors. In the figure, the step-shaped slopes in the traces are due to the fact that the data were logged with only a 2-digit precision. Higher precision would have resulted in smoother, harmonic curves.
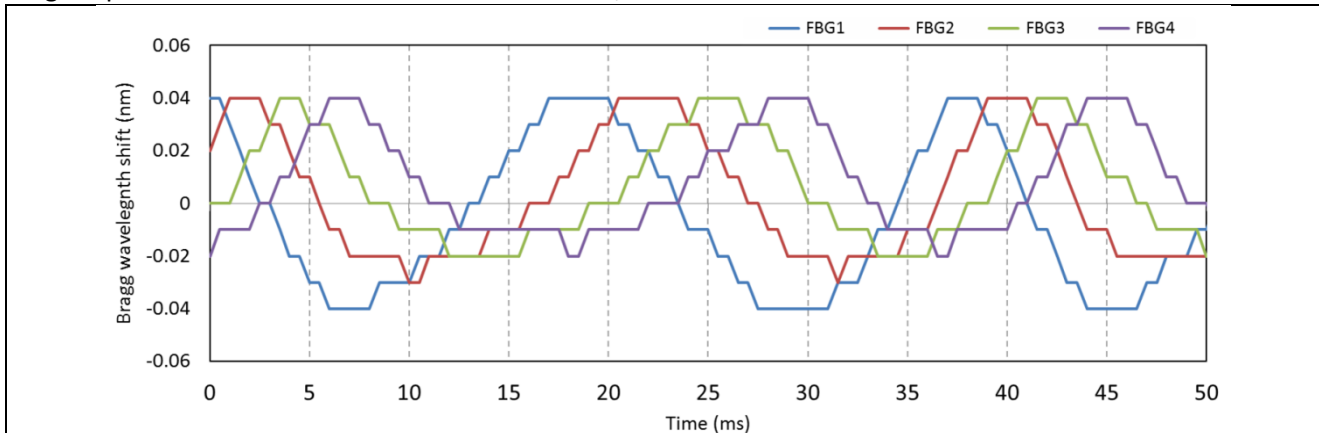

Figure 2.16 Dynamic responses of the first four circumferentially mounted FBGs on the PMAC motor, also showing a consistent phase shift between them.

- Successful creation of the all-in-one multi-parameter sensor system, coupled with a user-friendly interface.

Figure 2.17 shows the detailed sensor installation topology both onto the surface of a rotor (a) and on the inner surface of the stator (b) in order to achieve the integration of all the sensors, allowing for multi-parameter measurement. The sensor data obtained are processed using algorithms established based on a set of calibration data and the measurement results obtained are displayed using a user-friendly interface.
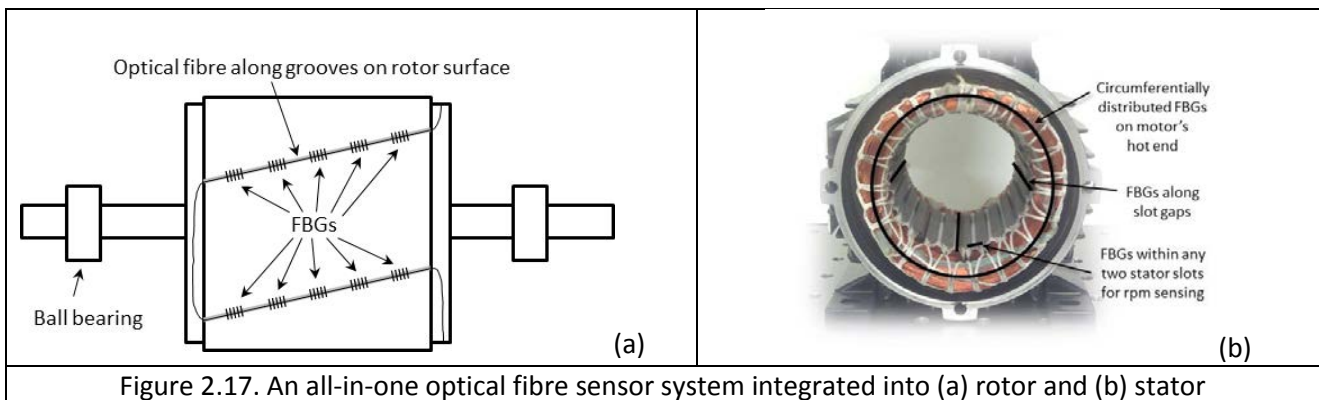

Figure 2.17. An all-in-one optical fibre sensor system integrated into (a) rotor and (b) stator

WP3 Integration of the novel all-in-one sensor system into motor drives
Deliverable 3.1 (Completed). Critical design review and report in integration of all-in-one sensor system into motor drive

Successful integration of the all-in-one sensor system into an induction motor, using 3 fibres connecting to 30 sensing points (FBGs) mapped inside an induction motor drive (rotor and stator), has been successfully achieved. Its critical design review and report is shown in Table 3.1

Table 3.1 Design review and report in integration of all-in-one sensor system into motor drive
The key aspects required to be considered to ensure appropriate sensor integration into a motor drive have been reviewed and summarized as follows: a.   Epoxy suitable for sensor integration

Due to space constraints within any electrical motor, as shown in Figure 3.1.1 (a), a typical distance between rotor and stator is < 1 mm, therefore there is not much room allowing for any sort of sensor packaging but to integrate directly the sensors into the motor using epoxy. It is, however, very important to choose the 'right' epoxy, as its shrinkage after being cured could lead to the reflection peaks of bare FBGs to split as shown in Figure 3.1.1 (b). Therefore, a suitable resin has to be used in the sensor integration. Table 3.1.1 lists the key parameters of suitable varnishes used for motor winding impregnation and the intention of choosing these epoxies for evaluation is to integrate the sensors at the manufacturing stage of the motor.
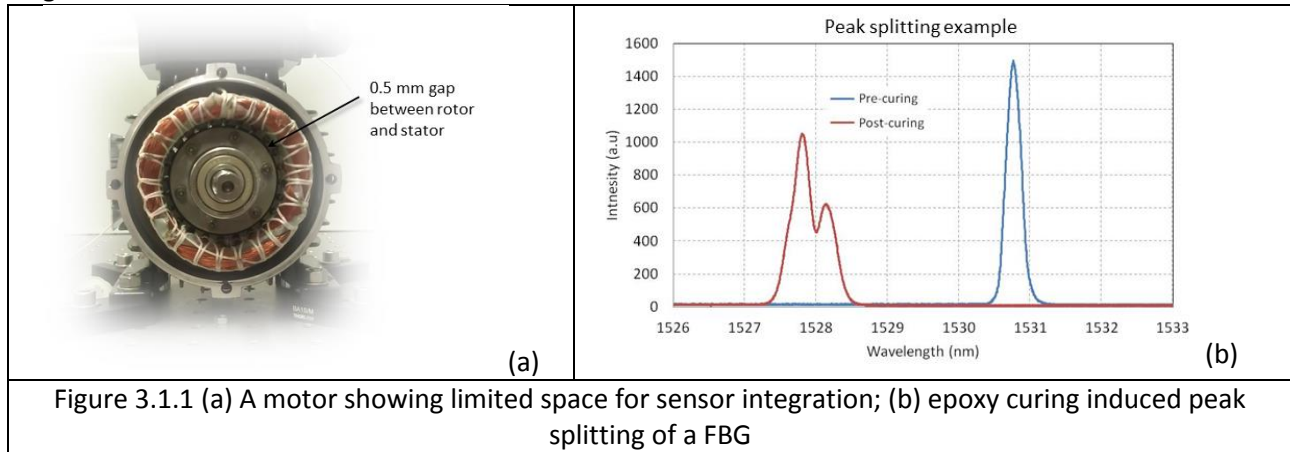

(a)   (b)

Figure 3.1.1 (a) A motor showing limited space for sensor integration; (b) epoxy curing induced peak splitting of a FBG

Table 3.1.1 List of recommended high temperature epoxy for sensor integration			
	Epoxylite TSA 220	Epoxylite 235 SG	Wacker Silres H62
Type	1-Component	2-Component	1-Component
T$_{max}$ (°C)	220	180	>200
Curing schedule	12 hrs @ 165 °C	30 min @ 60 °C 1 hr @ 130 °C	8-12 hrs @ 200 °C

In order to verify their suitable for the sensor integration, extensive tests have been undertaken and Table 3.1.2 shows the summary of the peak splitting tests on the FBGs written in different photosensitive fibres.

Table 3.1.2 Peak splitting tests on FBGs written in different photosensitive fibres			
(The numbers indicate *split peaks / number of tested FBGs*)			
Resin	**PS1550-125**	**SM1550-125**	**SM1550-50**
TSA220	0/10	5/10	7/10
235 SG	0/10	0/10	0/10
Silres H62	0/18	- / -	- / -

Both the *Silres* and *235 SG* have shown the promise. However, *Silres* resin has been specifically chosen and been used throughout this project because it is a single-component resin and is the preferred option of the motor manufacturer.

b. Rotor shaft signal coupling

The sensors are not just integrated into the stator, but also the rotor, therefore it is essential to ensure the signals obtained from rotor shaft to be reliably transmitted to the FBG interrogator. This is achieved via a key component, termed fibre-optic rotary joint (FORJ), which enables the physical connection between the static and rotary parts. Figure 3.1.2 shows a commercial FORJ which has been used in this project and used for the rotor sensor integration. This commercial FORJ (Princetel RFCX series) allows for rotational speed up to 2,000rpm.
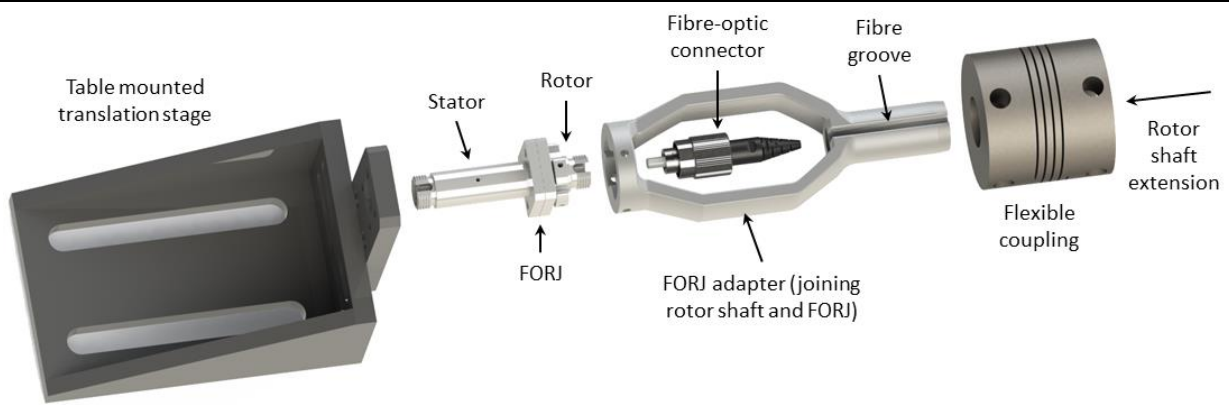
Figure 3.1.2 Fibre-optic rotary joint (FORJ) used to couple the sensor signal out of the rotor shaft

As an alternative approach for the rotor interrogation, a non-contact solution was investigated using lenses instead of a mechanical rotary joint. As illustrated in Figure 3.1.3 (a), a number of lens configurations were tested using high-precision translation stages. A 'GRIN-Convex-Concave-GRIN' lens system configuration was found to provide an acceptable level of optical losses while offering a small degree of rotor shaft eccentricity and no real limitation in terms of rotational speed. The lens system is shown in Figure 3.1.3 (b). In the transmission case, the GRIN lens on the left increases the beam diameter of the incoming light of the single mode fibre (coming from the sensing interrogator). This enhanced and collimated beam is then converted into an expanding cone by a convex lens. On the receiving end, the cone is collimated by a concave lens to be focused into the sensing fibre by another GRIN lens. The reflected signal (coming from the FBG sensors) passes the same optical path but in reverse direction. However, compared to the mechanical rotary joint as shown in Figure 3.1.2, this configuration requires very precise alignment and is sensitive to mechanical vibration.
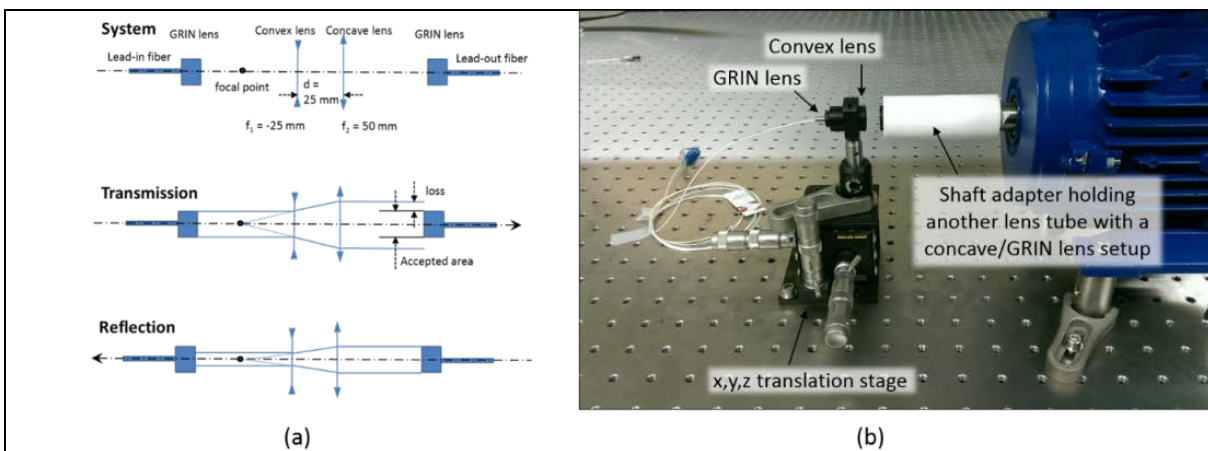

Figure 3.1.3 Non-contact rotatory joint (a) lens configurations; (b) photo from City University London

c.   Rotor instrumentation

One typical example of rotor instrumentation is shown in Figure 3.1.4 (a), in which 17 FBGs, acting as distributed temperature sensors, are written into bend-insensitive fibre (Fibrecore SM1500) and multiplexed using wavelength division multiplexing technique before being installed on the surface of the rotor. The fibre routing, however, as shown in Figure 3.1.4 (b) is via a groove beneath the ball bearing to make the measurement non-destructive.
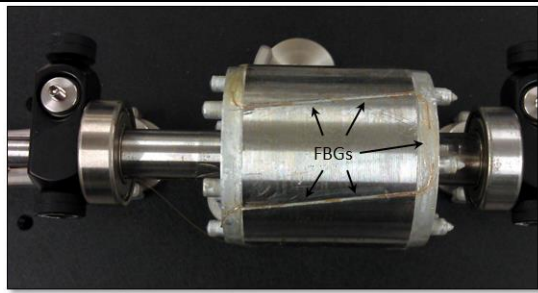
Figure 3.1.4 (a) Instrumentation of an induction machine rotor with 17 FBGs; (b) Fibre routing

d.   Integration of an all-in-one sensor system into an induction motor drive

Figure 3.1.5 shows a SMART motor drive which is integrated with an all-in-one fibre sensor system. It is also connected to conventional sensors, e.g. torque meter and speed sensor, for cross-comparison. When the rotor is operating at different working conditions, e.g. driven at different speeds, under varying loading conditions and driven at different torque levels, a very good agreement has been reached between the optical and conventional sensors although the latter is required to be installed externally and well 'protected'.
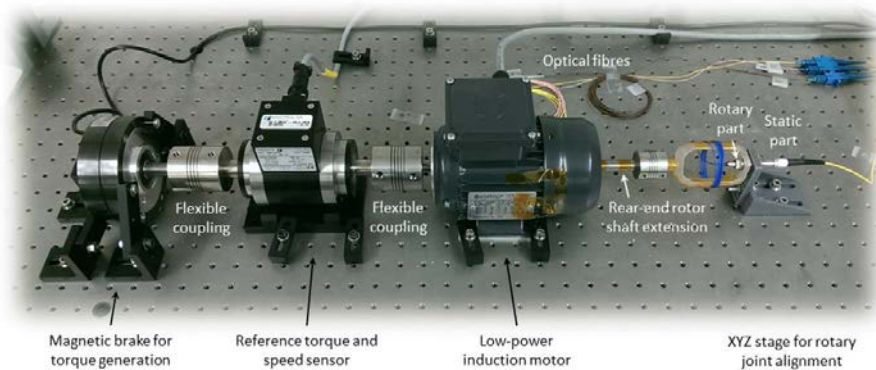
Figure 3.1.5. Smart motor drive integrated with both optical fibre sensors and conventional sensors

WP4 Sensor data usage and display

Deliverable 4.1 (completed). Demonstration of SMART drives with the sensor data being used for reliability monitoring and ready to be integrated into control software.

A user-friendly interface is designed and developed in LabView™ using the in-built VISA (Virtual Instrument Software Architecture) functions for device communication, i.e., command and data transfer between PC/Laptop and the optical sensing interrogation unit. A total of *three* applications was developed; (i) an application to inspect the FBG reflection spectra which allows for the determination of the appropriate peak detection parameters and to track/log the Bragg wavelength shifts for calibration purposes, (ii) an application to process calibration data, i.e., to extract the calibration parameters from the raw data, and (iii) the main application to monitor/process/visualise/log the motor data in real-time.

Figure 4.1 shows a screenshot of the FBG inspection/tracking application with the actual FBG reflection spectra of the instrumented motor being shown. The colours in the spectral diagram in Figure 4.1 represent different channels and it can be seen that all 12 FBGs on each channel are successfully detected by the peak detection algorithm. In the case of erroneous data being acquired by the main motor monitoring application, this application can be used to inspect the state of the reflection spectra as a first measure. Also, different sets of peak detection parameters can be tested here to enhance the reliability of the peak detection.
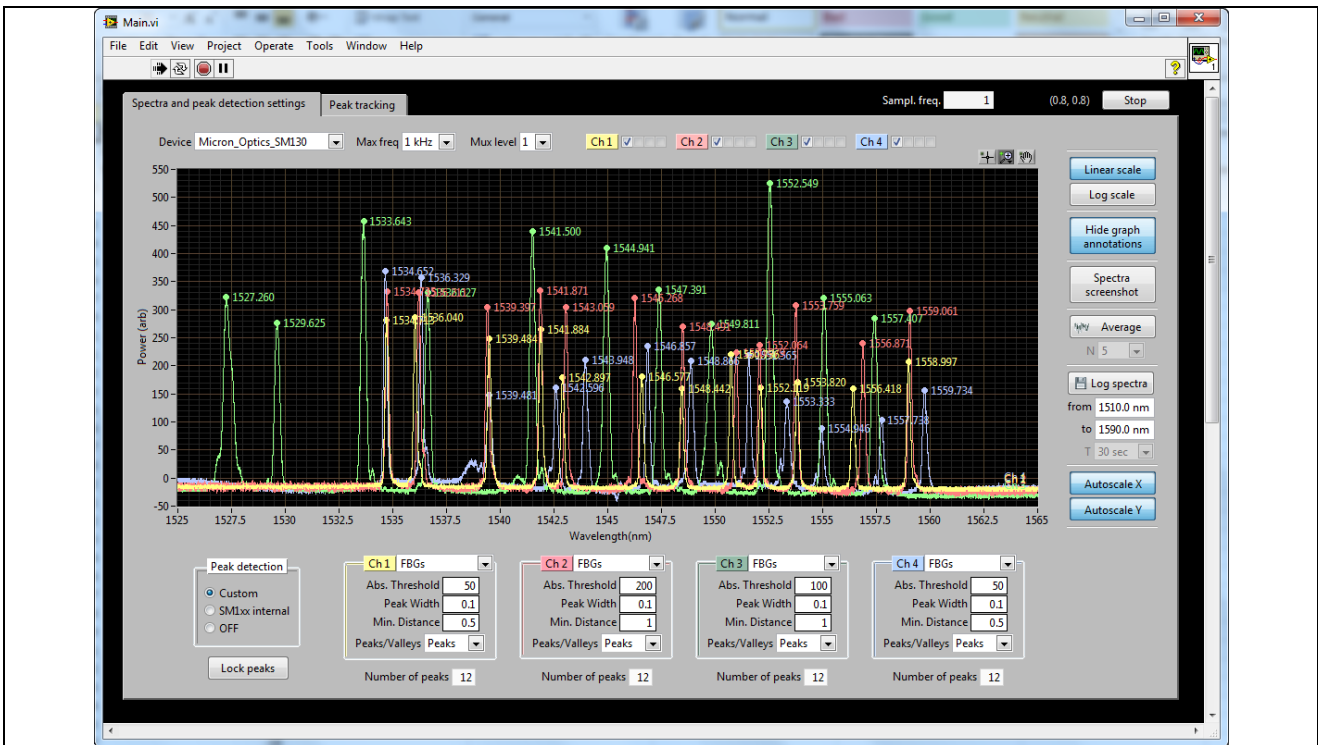
Figure 4.1. Screenshot of the application used to inspect the FBG spectra of the fibres the motor was instrumented with.

Figure 4.2 shows a screenshot of the peak tracking interface of the same application which can be used to assess the sensor stability or to log data for calibration purposes. Individual traces can be visually inspected at runtime by selecting the sensor(s) of interest from the lists on the right. The logging function allows for the continuous storage of real-time data if post-processing is required, for calibration purposes for instance. The data shown in the figure is from a random set of FBGs.
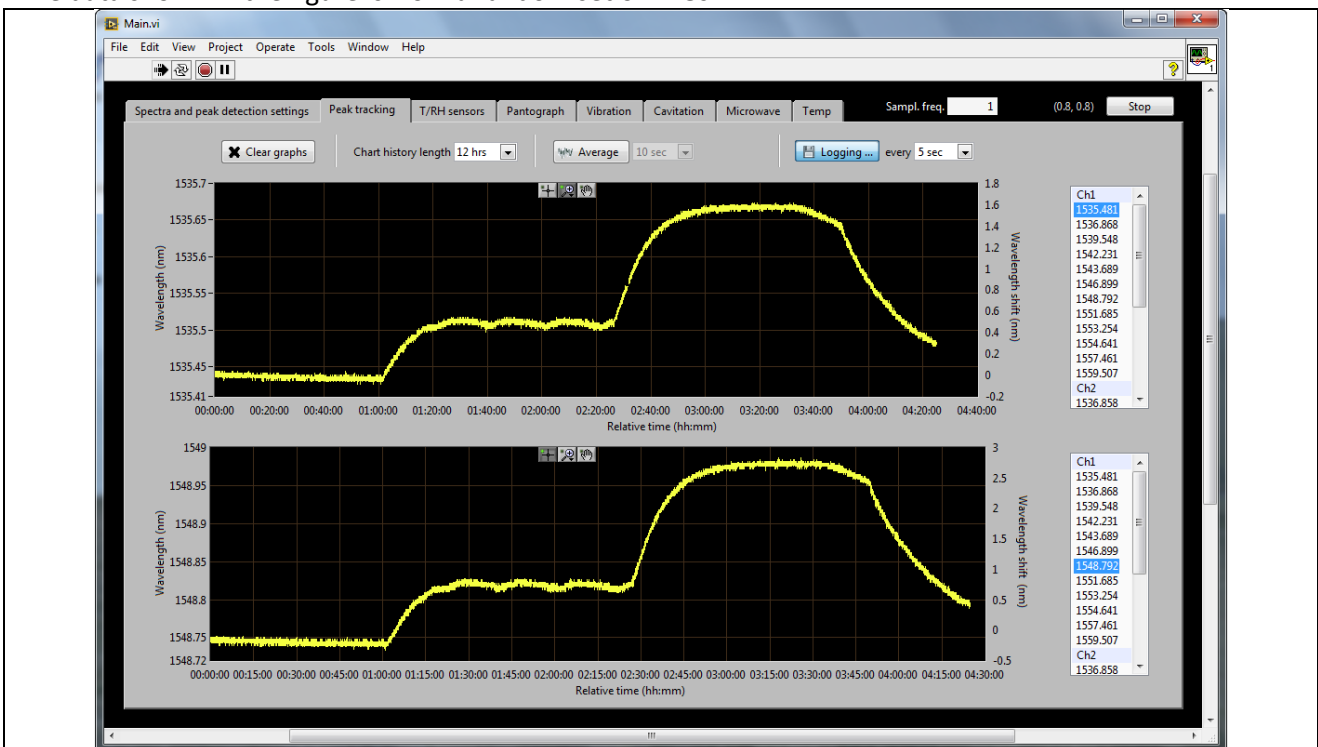
Figure 4.2. Screenshot of the peak tracking tab of the FBG inspection application.

Given the large number of sensor elements, a second application was developed to process calibration data efficiently. A data file, recorded with the peak tracking application, can be loaded into this application and

the file content is being displayed as shown in Figure 4.3. The data shown are the actual Bragg wavelength shifts from the temperature calibration in Figure 2.7.
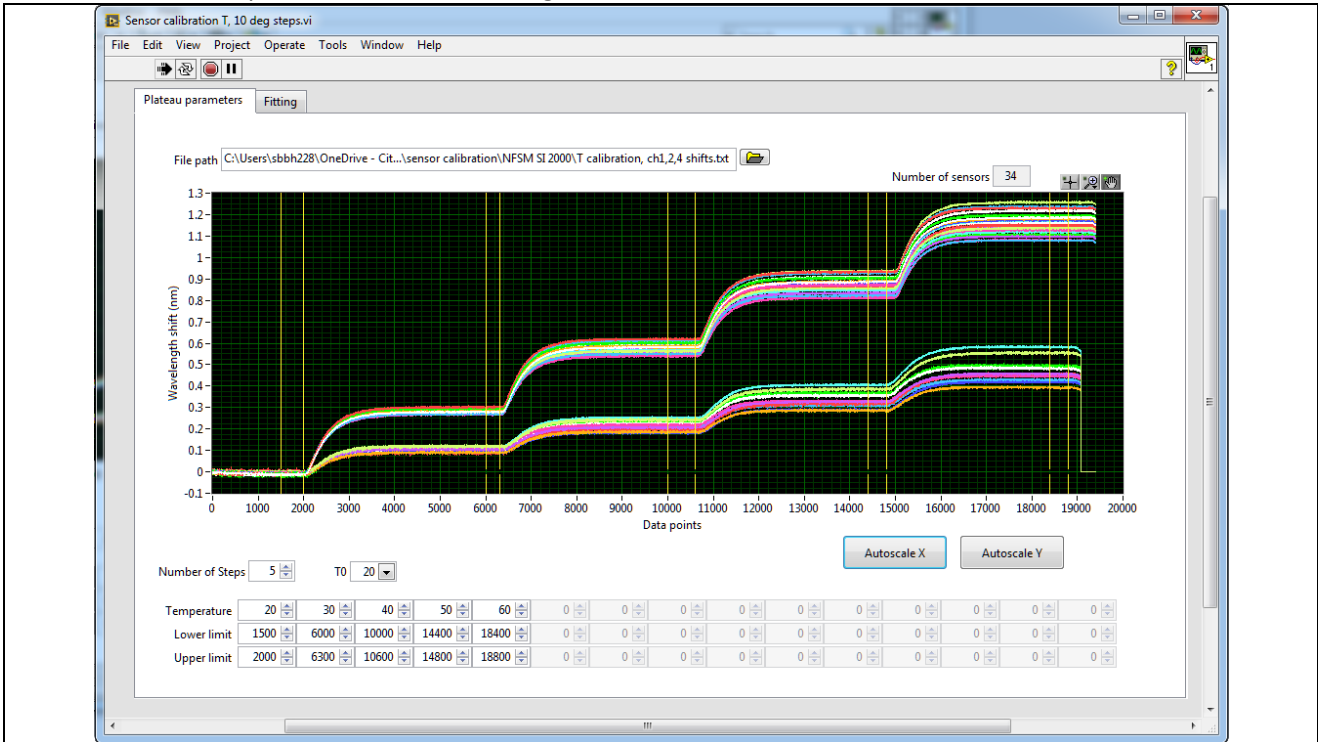

Figure 4.3. Screenshot of the application developed to efficiently process calibration data.

The data sections meant to be used for the calibration can be marked (shown by the yellow vertical markers) and the software then extracts those sections and averages the data (individually for each trace). Those averaged points are then fitted as shown in Figure 4.4. The fitting curves together with the corresponding fitting parameters and quality of fit coefficients are visually presented by the application in order to easily identify potentially erroneous data.
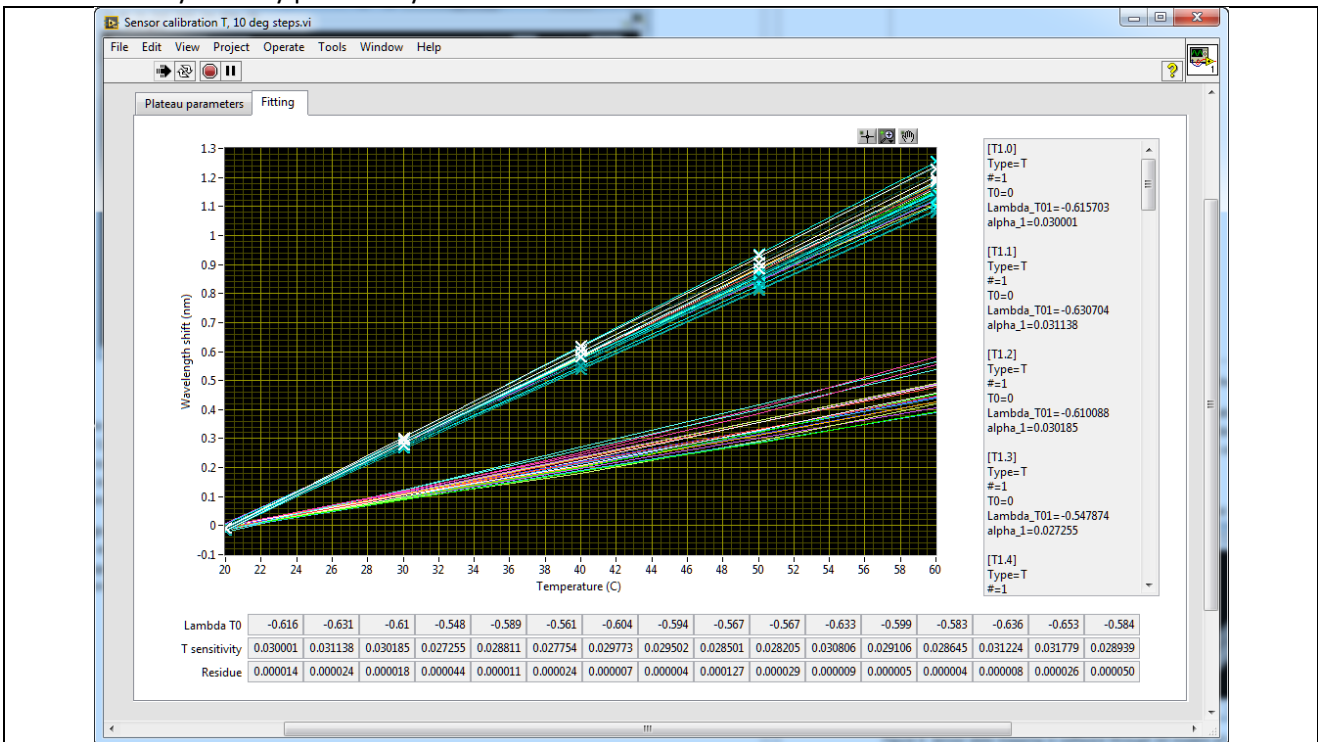

Figure 4.4. Visualisation of the fitting curves and corresponding parameters.

The third and main application developed in this project is the motor monitoring application, visually presenting the parameters of interest as well as offering the option to log the data. For the PMAC motor, a total of 39 parameters is being monitored and processed in real-time, 35 temperature values (24 on the

stator end-windings, 10 on the rotor magnets and one on the shaft), rotor speed, stator vibration, torque and the rotor position, the latter not being shown on the GUI (Graphical User Interface) as it is reserved for future use in a control loop. When logged, each data set is tagged by a millisecond timestamp. In order to provide maximum user friendliness of the monitoring application, the software does not require or demand any user input or manual configuration to function. All checks and hardware configurations are done automatically before the data acquisition starts. Therefore it does not require the end user to have any prior knowledge of the sensing principle or the deployed hardware.
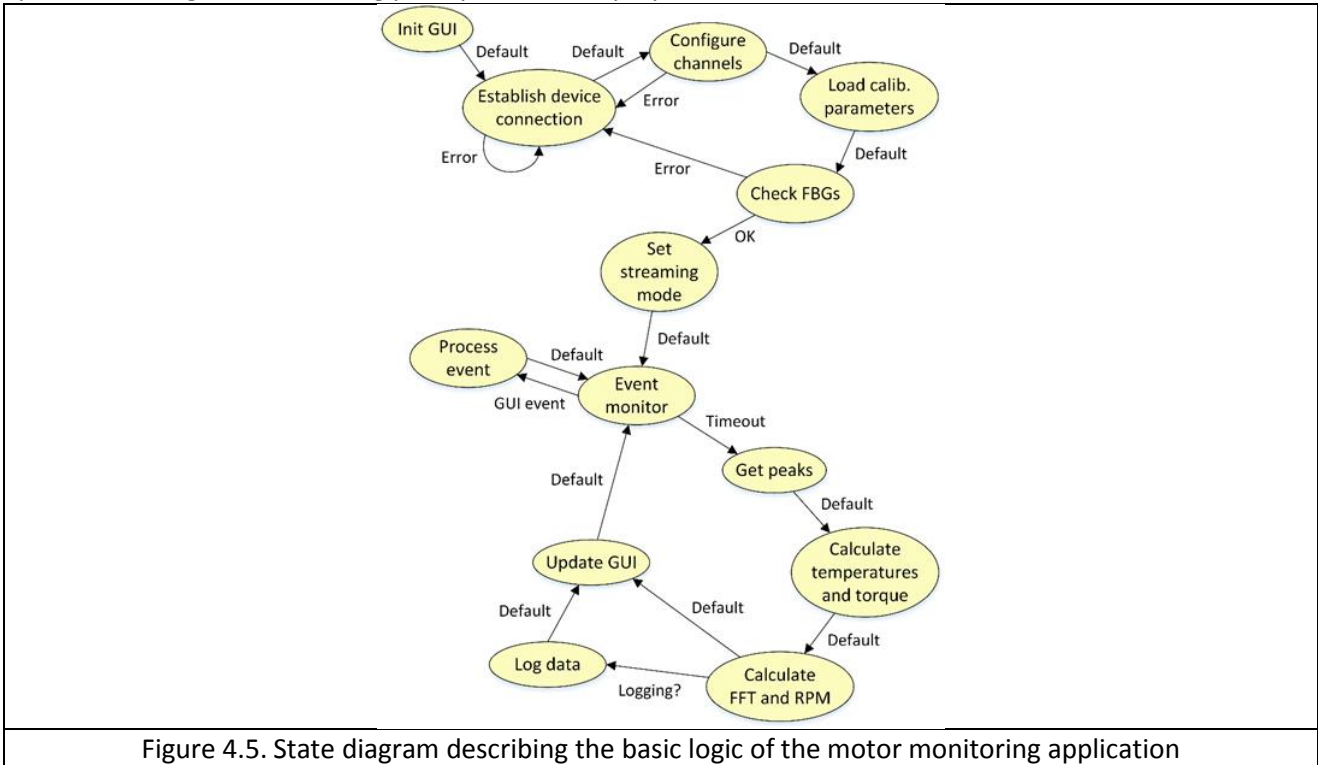

Figure 4.5. State diagram describing the basic logic of the motor monitoring application

The software architecture was chosen to be a so-called "state machine" which makes it possible to break down the code into small functional blocks, increasing readability and making it easier to edit or add blocks of code without affecting others. It also provides the ability to implement decision making algorithms by only executing sections of code needed in a particular situation, e.g., establishing a device connection or loading a calibration parameter file. The state diagram in Figure 4.5 shows the basic code structure. In the figure, the states (oval nodes) describe the actions executed when the state is called, whereas the transitions (arrows) describe when and how the process moves from one stage to another.

When running the application, the first step is the GUI initialisation. All user controls, diagrams, buttons etc. are set to a default state. Next, a communication link between the PC and the sensing interrogator unit is established and the device is initialised to the required operating condition (setting the sampling rate, for instance). Once completed, the channels are being configured, i.e., they are being enabled and the gain and threshold levels for the peak detection are set. This is the most vital part of the initialisation procedure because if the channel settings are not set to the required values the peak detection will be corrupted and with it the sensor data. Therefore, if an error occurs during this procedure, the communication link is being re-set and the device re-initialised. When the hardware was successfully configured, the FBG calibration parameters are loaded into memory from a text file for later use. Before activating the streaming mode (continuous output of the peak wavelengths by the sensing interrogator), a final check is performed on whether all sensors are being successfully detected. If not, an error message on the GUI informs the user of the nature of the problem, i.e., on which channel(s)/fibre(s) a problem was detected. After the check is passed and the streaming mode activated, the software sits in an endless loop of reading the FBG peak wavelengths and extracting the desired information (temperatures, rpm, torque, etc.) through a number of data processing algorithms, developed specifically and built in the software. This data acquisition loop is only interrupted in case of GUI events, i.e., a button being pressed, a configuration parameter being

changed etc. In that case an event handler is called and depending on the source of the event, the appropriate routine is executed before returning to the data acquisition loop. The event handler also includes routines to terminate the application or pause the data transfer in which case the software does not return to the data acquisition cycle.

The motor control software accepts data obtained from quadrature encoders which provide two phase-shifted (90 degrees) square waves that are used to determine the position and velocity of a rotor as well as the spin direction. This data set can now be replaced by a more comprehensive set of data obtained from the FBG-based sensor network, providing not just rotational information, but also temperature, torque and vibration, made compatible with the control software by squaring the trace data obtained from the FBGs.

WP5 Development of a generic demonstration test bed
Deliverable 5.1 (completed). Installation and commissioning of a demonstration test bed which includes the motor drive under test and load drive, integrated with both optical and conventional sensors.

Further to the successful integration of the novel all-in-one sensor system into a low-power induction motor, as shown in Figure 3.1.5., a PMAC motor, provided by the University of Nottingham, was subsequently instrumented with a total of 48 FBG sensors mapped over four fibres with 12 FBGs each. The fully instrumented machine is depicted in Figure 5.1, further to the detailed illustrations of the PMAC rotor instrumentation in Figure 2.3 and of the PMAC stator in Figures 2.5 and 2.13 respectively.
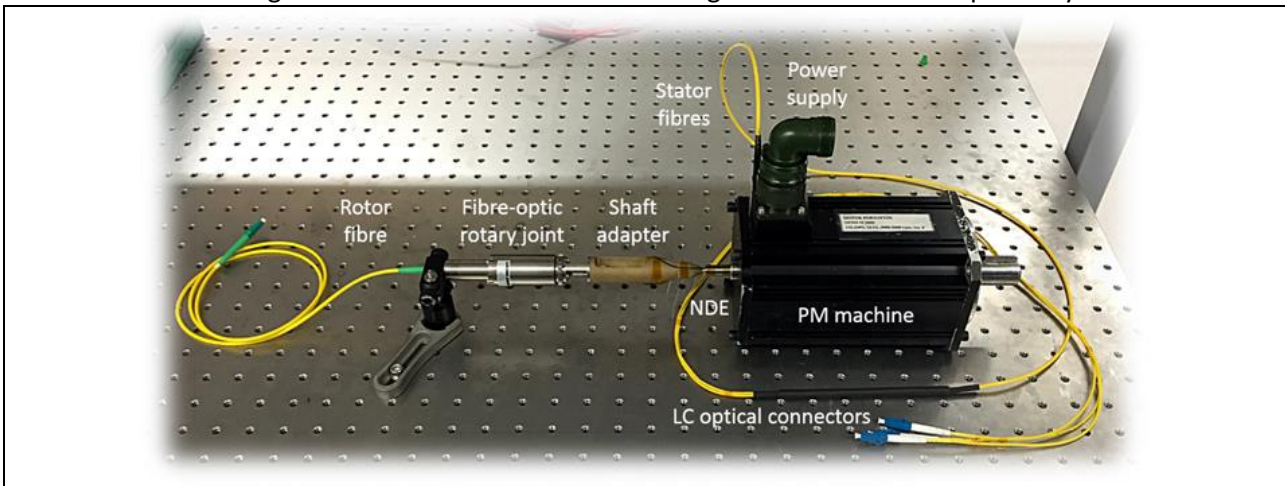

Figure 5.1. PM machine instrumented with 48 FBGs on 4 fibres measuring rotor speed, torque, vibration, the rotor magnet temperatures and stator end-winding temperatures.
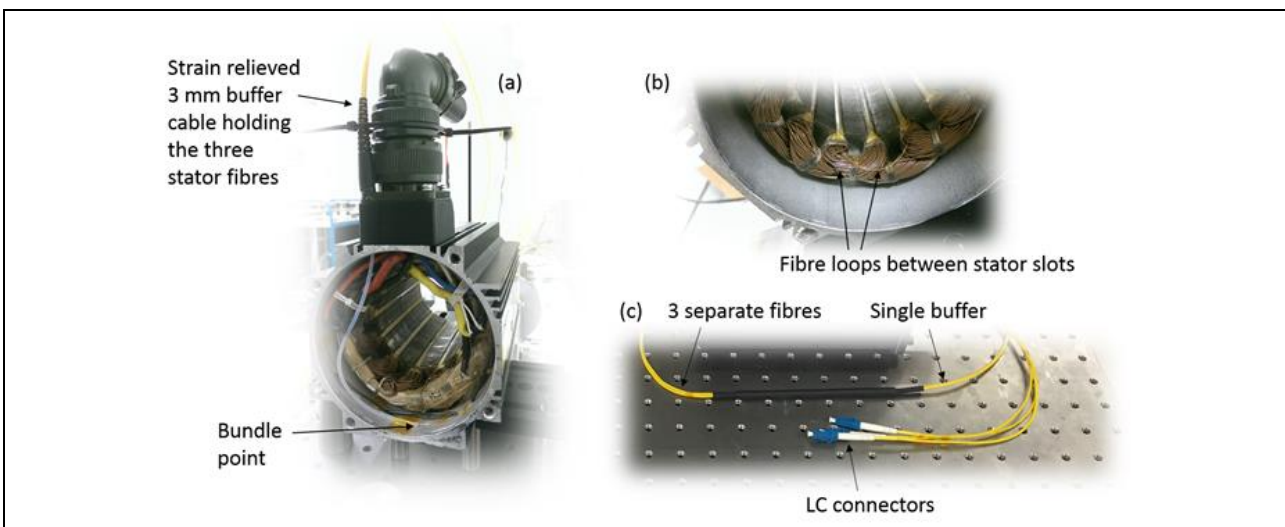

Figure 5.2. Stator fibre routing. The three stator fibres exit the motor through a single strain relieved buffer cable (a) and are then broken out to three separate fibres terminated with LC/UPC connectors (c). The fibre loops in between stator slots are shown in sub-figure (b).

Proper fibre routing is of prime importance for ensuring the whole sensor system to be 'alive'. The three bare stator fibres, i.e., the two end-winding temperature fibres and the rotor speed/position fibre, are bundled in a semi-flexible plastic tube inside the machine and exit the motor through a strain-relieved standard 3mm buffer cable, as shown in Figure 5.2 (a) before being channelled out into three separate fibres, terminated with LC/UPC connectors, as shown in Figure 5.2 (c). At that point the fibres can be attached to standard optical patch cords of whatever length is required (hundreds of meters if necessary). The fibre loops in between stator slots are shown in Figure 5.2 (b).

For ease of fibre routing on the PMAC rotor, tiny grooves were also machined into the rotor collars at either end to safely route the fibre from the magnets on to the shaft. The fibre then exits the rotor through another groove beneath the bearing and the encoder at the motor's non-drive end as shown in Figure 5.3.
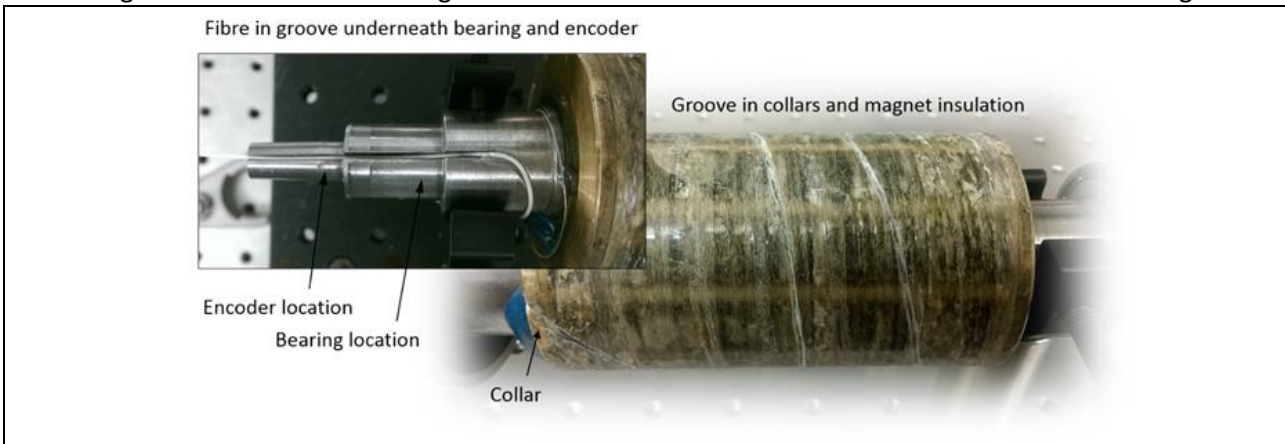

Figure 5.3. The sensor fibre routed along grooves on the rotor and shaft surface

In order to continuously monitor the FBGs on the spinning rotor, a fibre-optic rotary joint (Princetel MJX series, 10,000 rpm) was also attached to the rotor via a specifically designed shaft adapter as depicted in Figure 5.4. The shaft adapter is threaded into the rotor's non-drive end and the other end slots into the rotary joint. The stationary part of the rotary joint is clamped to a solid surface using standard opto-mechanical mounts (posts, pillars, clamps).
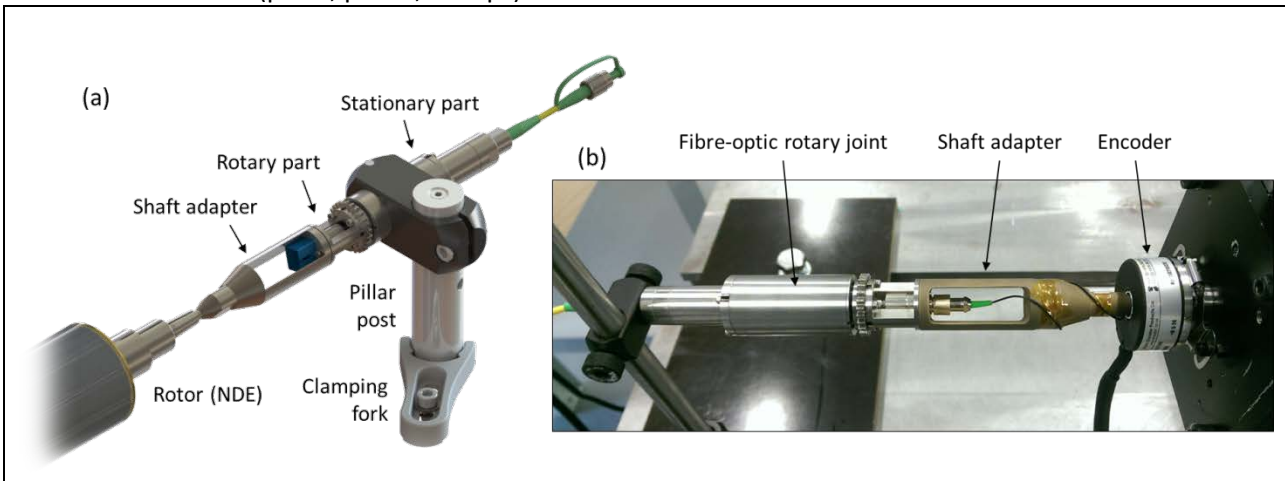

Figure 5.4 (a) Schematic representation of the 'rotor – shaft adapter – rotary joint' assembly for the PMAC motor. (b) Photograph of the assembly on the developed test rig.

The test bed was set up at the Institute for Aerospace Technology on the University of Nottingham's Jubilee Campus. The basic test bench components remained the same as in the original specifications and are shown in Figure 5.5.
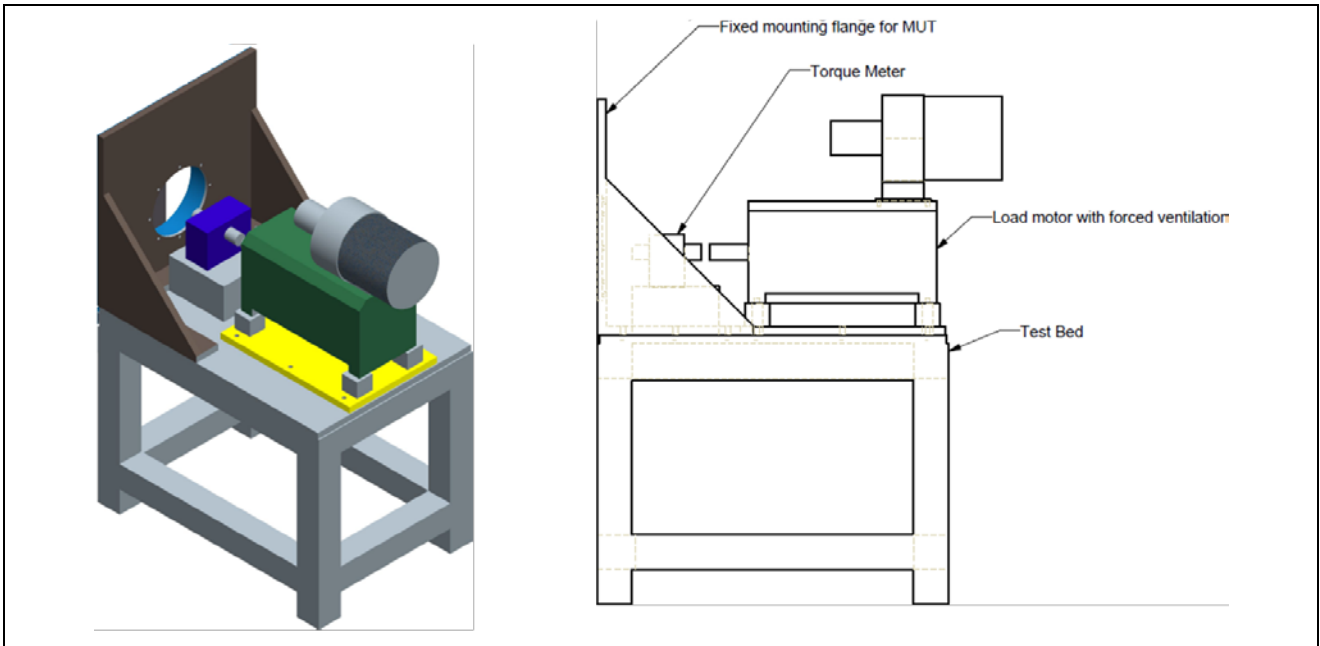
Figure 5.5. Schematic of the motor test bench and its respective components (drive components not shown).

The test bed, or frame, the angle plate and mounting flange were manufactured by a local company in Nottingham (Goodman Metal Works). The load motor was purchased from City Rewinds and Drives, and its corresponding 55 kW drive cubicle from Emerson Industrial Automation which also includes the drive for the PM machine. The torque transducer and couplings were sourced from Magtrol and smaller bits and pieces (encoder, cabling, bolts, etc.) from standard suppliers in the field. The test bench, as shown in Figure 5.6, was thus assembled and commissioned by the technical team at the University of Nottingham who also made the shaft guard. As shown in the figure, the test bench includes the PMAC motor drive under test and load drive, integrated with both optical and conventional sensors.
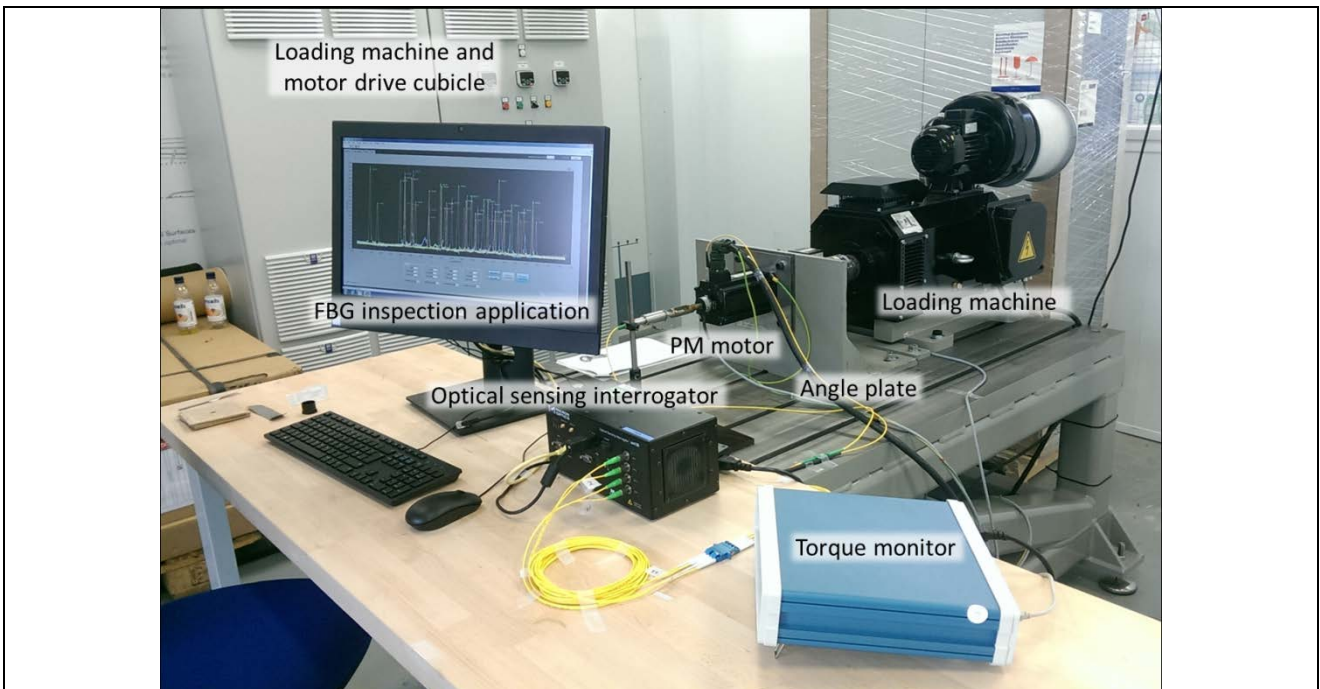

Figure 5.6. Photograph of the assembled test bench and corresponding instrumentation hardware at the Institute for Aerospace Technology, Nottingham University.

Figure 5.7 shows the test bench with an installed guard covering the rotating parts. The guard serves two purposes: (a) preventing persons from touching the rotating parts and (b) protecting surrounding equipment and persons from potentially loose parts. The guard was made from a transparent Perspex-like material that, in contrast to Perspex, does not shatter or burst upon impact. The figure also shows the torque transducer location in between the loading machine on the right and the PM motor on the left. The shafts were laser-aligned by the technical staff.
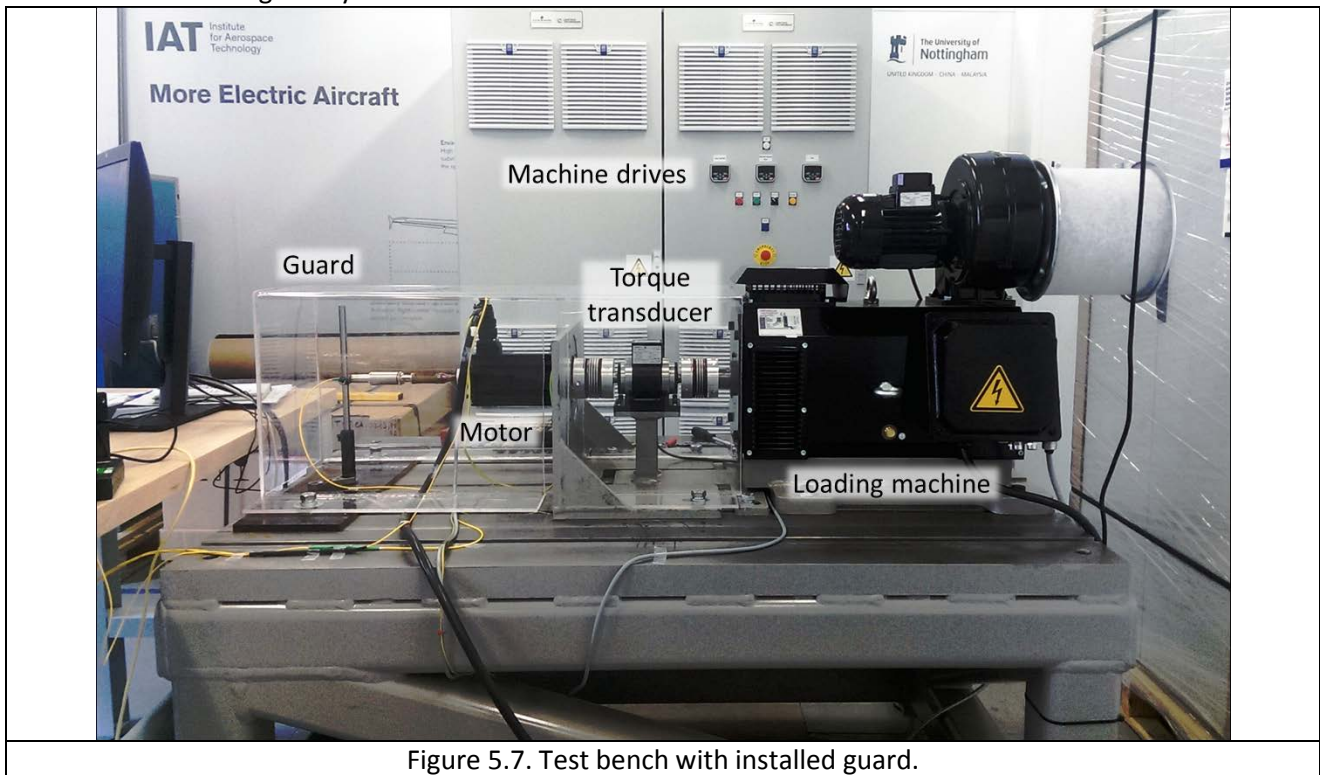

Figure 5.7. Test bench with installed guard.

WP6 Validation of the integrated test bed through extensive evaluation tests

<u>Deliverable 6.1 (completed).</u> Performance review and reports to Clean Sky Programme Manager and delivery of the test bed to the Topic Manager's Institution.

The performance review and reports to Clean Sky Programme Manager have been completed and ready for submission. The test bed was delivered to the Topic Manager's institution and was commissioned by local technical staff as detailed in WP5. This is followed by the extensive evaluation tests to validate the integrated test bed and the results obtained have shown great promise for both the Topic Manager's Institution and the EU aerospace industry to access to evaluate various types of aerospace motor drives under the circumstances as the machine used in real world.

Figure 6.1 shows a typical screenshot of the motor monitoring application GUI at runtime. The top left graph shows the stator end-winding temperatures versus time and the rotor temperatures are shown in the graph below it. The temperature data are also visualised on the right in the form of colour coded 3-D models of both the stator and the rotor. The two graphs in the centre show the torque data and rotor speed. The latter is extracted from the spectral response of one of the circumferentially mapped FBGs. The vibration signature of the machine is shown in the bottom graph. In the shown case, the first spectral feature corresponding to the mechanical rotor frequency (rotor speed) and the second feature to the stator wave frequency. The FFT window length can be changed with the resulting frequency resolution being shown above the graph. The buttons in the top right to pause the data acquisition, to log the data and to terminate the application and are self-explanatory. In addition to the data logging function, the contents of each graph can be exported to Excel at runtime with only two mouse clicks. This GUI design has been made flexible and can easily be edited by the end user to accommodate possible changes in the testing environment required by industry.
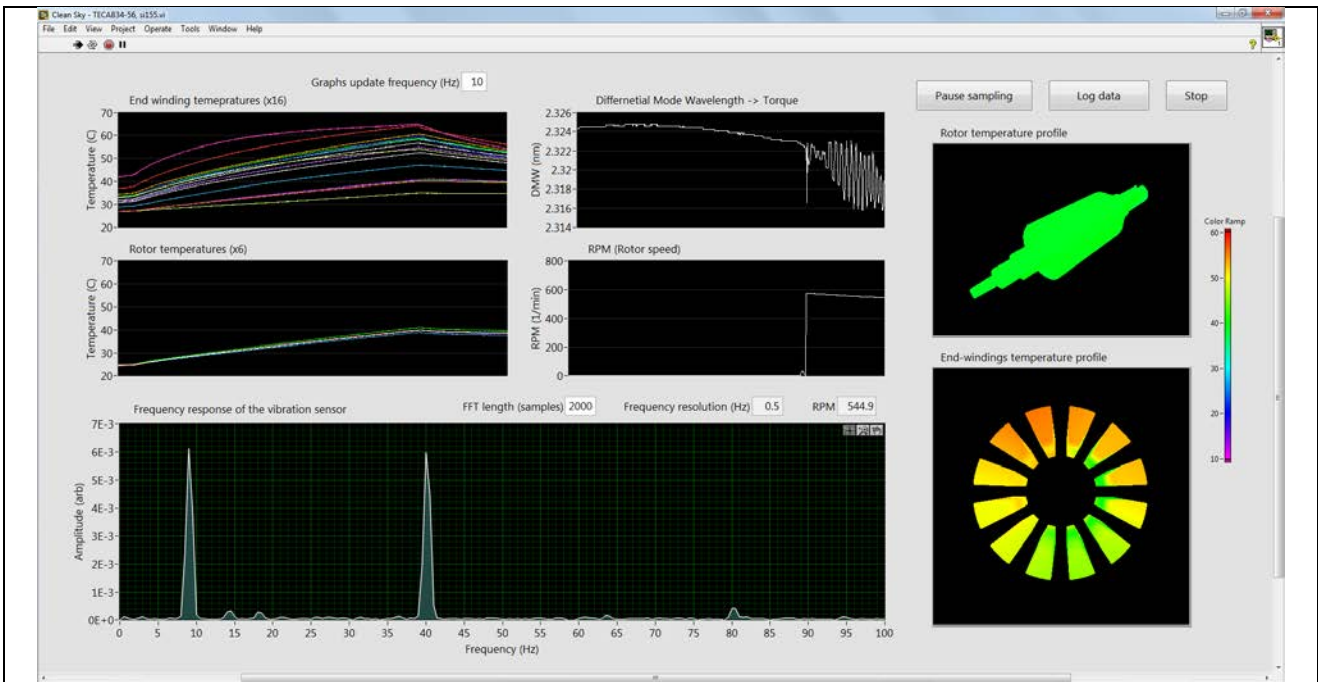
Figure 6.1. Screenshot of the motor monitoring application at runtime showing key motor parameters.

Figure 6.2 shows temperature data mapped in a 3-D format for both the rotor and stator as included in Figure 6.1. In the mapping configuration window of Figure 6.2, the sensor locations were marked on the model surface and a 1-D array containing the temperature data is wired to the VI. The algorithm developed has been validated by using fibres of identical FBG layout as the ones used in the motor that were locally heated. Figures 6.2 (a) and (b) show the resulting screenshot of the 3-D real-time visualisation. The data obtained are also managed and prepared for the next-stage integration into the motor control software.
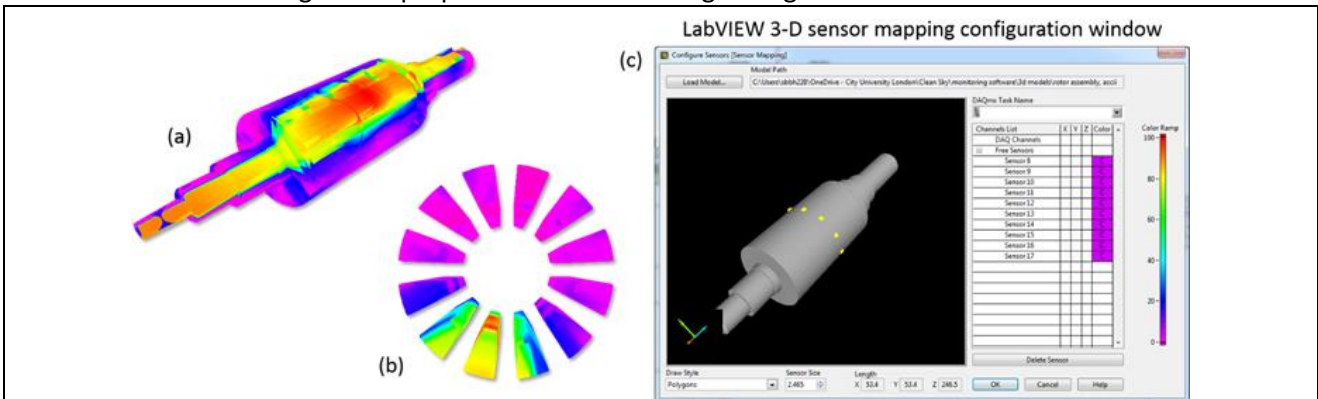

Figure 6.2. Sensor data mapping in software through 3D models of rotor and stator. (a, b) Localised heating of fibres of the same sensor layout as the actual ones attached to the rotor and stator end-windings to evaluate the mapping algorithm. (c) Sensor mapping configuration window in LabVIEW™.

In addition to the above successful completion of all the WPs laid out in this project, City University London has worked together with the University of Nottingham to explore jointly the potential of instrumenting the FBG sensors at manufacturing setting, rather than retrofitting, which would be more of the interest to manufacturers and to end users. Figure 6.3 (a) shows how the FBGs are packaged and instrumented into winding rather than being surface mounted before being integrated into the high power density motor shown in (b). Figure 6.4 (a) shows the instrumented motor drive with 16 FBGs and 3 RTDs with their cross-comparison results being shown in (b), confirming that a very good agreement having been reached, showing promise for next-stage commercial exploitation.
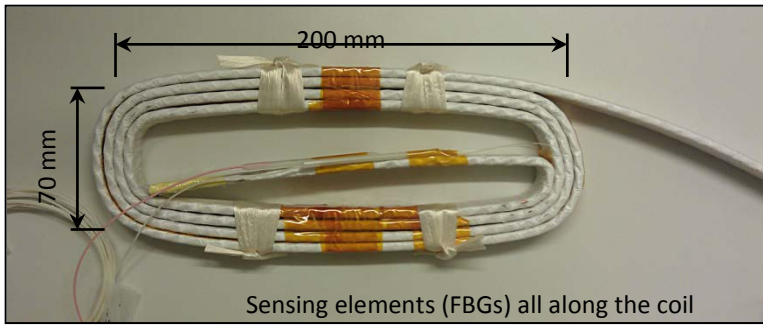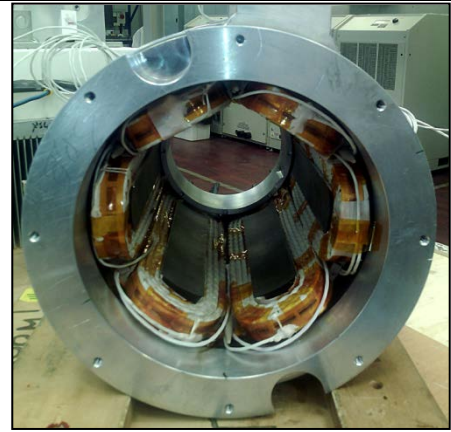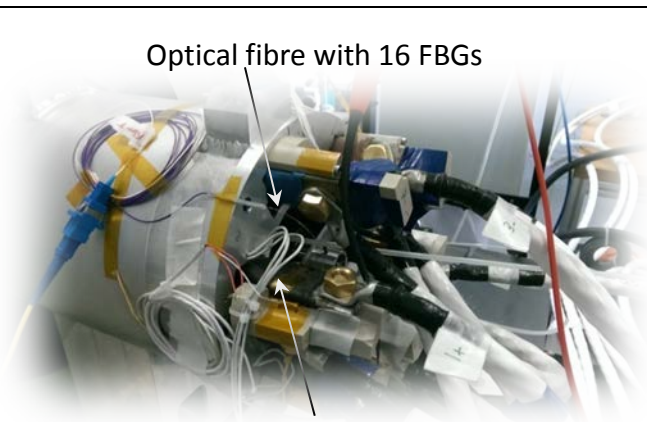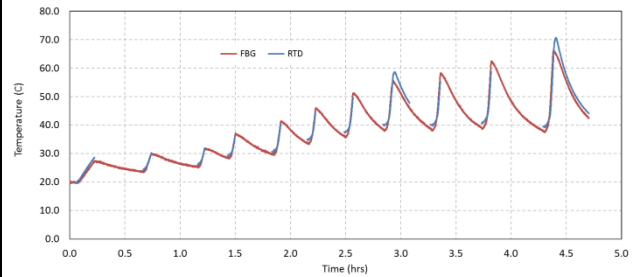
Figure 6.3. (a) Stator winding instrumented with FBGs; (b) High power density motor at Nottingham University

Figure 6.4. (a) High power density motor instrumented with FBGs and RTDs; (b) Cross-comparison of the results obtained from co-located FBG and RTD with the machine having been repeatedly loaded to generate some – increasingly steep, i.e., higher loads – temperature gradients.